Hardin, R.A., and Beckermann, C., "Simulation of the Mechanical Performance of Cast Steel with Porosity: Static Properties," in Proceedings of the 60th SFSA Technical and Operating Conference, Paper No. 4.3, Steel Founders' Society of America, Chicago, IL, 2006.

# Simulation of the Mechanical Performance of Cast Steel with Porosity: Static Properties

R.A. Hardin[1] and C. Beckermann[2]

[1]Research Engineer, Mechanical and Industrial Engineering Dept. The University of Iowa
[2]Professor, Mechanical and Industrial Engineering Dept. The University of Iowa

## Abstract

As designers look to lighter-weight, thinner-walled steel castings, knowledge of the location, amount, characteristics and effects of porosity on properties is more critical than ever. In the work presented here, a method for incorporating the effect of porosity on steel stiffness (elastic modulus) is presented, and simulations using the method are compared with experimental measurements. Here x-ray tomography is used to determine the specimen porosity distribution. The porosity distribution is imported into finite element simulations where the elastic modulus and Poisson ratio are dependent on the porosity field. A relationship between elastic modulus and porosity is determined through comparison between finite element simulations and measurements. It is found that steel exhibits a critical porosity level, when porosity exceeds this level the material essentially looses all stiffness or load carrying capability. The elastic modulus decreases non-linearly with porosity. An equation relating elastic modulus and porosity is found to give good agreement between measured and predicted elastic modulus for 8630 steel specimens with porosity. It is

$$E(\phi) = E_0 \left(1 - \frac{\phi}{0.5}\right)^{2.5}$$

where E is the resulting modulus of the material having porosity volume fraction $\phi$, and $E_0$ is the elastic modulus of the sound material. A review of literature on the properties of porous materials supports this finding. Results of this study and the literature reviewed reveal that the static properties of porous materials depend not only on the amount of porosity, but on how it is distributed and other characteristics such as pore shape and size. By modeling the effect of the porosity distribution in the FEA simulations, the material behavior is accurately predicted within ±10% agreement compared with measurements, and inhomogeneities due to porosity can be considered in part design.

# 1. Introduction

Many materials contain porosity, either in their natural forms (e.g. wood, bone, coral and rock) or as a result of their production (e.g. concrete, ceramics, composites, and metals). As a result, understanding the effects of porosity on the mechanical properties has long been recognized as important. It will be shown, through literature reviewed and based on the results of the present study, that the static properties (stiffness and strength), of porous materials depend not only on the amount of porosity, but on how it is distributed and other characteristics such as pore shape and size.

Porous materials such as ceramics, foams (metal or polymeric) and sintered metals are being applied in lightweight applications. For these materials the porosity may be designed into the material. The porosity is characterized by volumetric amount, size and shape of pores, cellular structure, and is typically homogeneous and uniformly distributed. Designing components from such materials appears to be relatively straight-forward once the material properties are established, and if local variations in the stress-strain field due to the pores can be ignored. For these porous materials, apparent (or effective) properties are sufficient for engineering design [1, 2], and there exist numerous theoretical and empirical methods to predict their properties.

In the case of cast metals, and steel castings in particular, every effort should be made to produce a sound, porosity-free casting. Still porosity may occur in a part which cannot be eliminated without unreasonable cost, making the part "casting unfriendly". If porosity forms in a casting, it will probably be localized and not uniformly distributed relative to the entire part, and the casting material properties are non-homogenous. For such cases, there are local effects of the porosity. When the actual stress-strain field is compared to the design/porosity-free field, stress-strain redistribution takes place in the part due to the pores, and uniform properties should not be assumed. Local plastic deformations may occur due to the pores, where the original porosity-free design may have shown only elastic-range displacement. Hopefully the porosity will be detectable by NDE, but microporosity may form that is undetectable. While microporosity may not result in much localized stress concentrations and stress redistribution, it can greatly affect fatigue resistance [3-6]. Casting process models can predict the likelihood of microporosity forming and can guide inspection criteria or allow the designer to simulate the possible effects of porosity on part performance. Macro-porosity in metals (often defined as porosity visible without magnification, typically > 100 μm) can cause gross section loss reducing the effective elastic modulus or stiffness [6]. Porosity in cast metal results in stress concentrations near pores, which can lead to localized plastic deformation and the development of microcracks which lead to failure.

It is not typical that inhomogeneities due to porosity are considered in part design, but the authors of this study and others [7-8] are developing methods that can consider porosity's effect on part performance. As designers look to lighter-weight, thinner-walled steel castings, knowledge of the location, amount of porosity, and effect of porosity on strength and fatigue behavior is more critical than ever before. In the work presented here, a method for incorporating the effect of porosity on steel stiffness (elastic modulus) is presented, and simulations using the method are compared with experimental measurements. A review of literature shows that the effect of porosity on strength properties may be predicted as well.

## 2. Review of Past Work

It has been recommended [9] that the physical relationships between porosity and properties such as stiffness and strength fall into three categories of behavior based on porosity level: 1) less than 10%, 2) 10% to 70%, and 3) materials with greater than 70%. Bear in mind, the ranges in the previous statement are approximate. Principally, the reasoning behind this division is that the materials at the two extremes 1) and 3) behave quite differently and are described using very different physical models. In addition to the amount of porosity, properties of porous materials also depend upon aspects of the porosity that can be hard to characterize and generalize [10-13]; such as pore geometry, size, shape, geometry of interconnections of solid, and arrangement of pores, just to name a few. Some of these hard to quantify aspects can be described as the *porosity distribution* or *how the porosity is distributed*. The review below is thorough, since it is not expected that steel foundry engineers or designers of steel castings are much aware of the literature reviewed. This review is organized by first examining work in the least porous category, then the most, and then the large middle range, which overlaps the extremes and is the area where the present work falls.

### 2.1 Effect of Low Levels of Porosity on Stiffness and Strength

Stiffness, or modulus of elasticity, of materials in the lowest range porosity range can be described by a linear dependence on porosity, derived with the assumption that voids do not interact [14]. An interesting comparison between experimental data up to 4% porosity for a cast Mg alloy, and theoretical models is given in Figure 1 [15]. The data appears linear in this range. Three theoretical relationships are compared with the data:

$$E(\phi) = E_0 \left(1-\phi\right) \tag{1}$$

$$E(\phi) = E_0 \left(1-1.86\cdot\phi+0.86\cdot\phi^2\right) \tag{2}$$

$$E(\phi) = E_0 \left(1-\phi\right)^3 \tag{3}$$

where E is the resulting modulus of the material having porosity volume fraction $\phi$, and $E_0$ is the elastic modulus of the sound material. Equation (1) is from the so-called "rule of mixtures", used in composite materials relating the elastic moduli and volume fractions of the two-phases in the material. It results when one of the two phases is a pore of zero elastic modulus [15]. Equation (2) is for material with spherical holes, first used by Coble and Kingery to describe the elastic modulus of porous alumina [16]. Equation (3) is derived by Maiti et al. [17] for closed-cell porous materials; note that the power "3" is replaced by "2" for an open-cell material. The data in Figure 1 appears to be within the bounds of these models, and the three models span a range of porosity structures.

Strength behavior in the lowest range of porosity, approximately less than 10%, appears adequately described by considering isolated pores (or voids) [18], or a uniform distribution of pores [19], and the single state variable needed in these models (other than model constants or parameters) is the volume fraction of porosity (or relative density). These are so-called "micromechanics" models. Probably the best known example of such a model describing the plastic behavior of "mildly voided" [20] materials is the porous metal plasticity model available

in the finite element analysis software ABAQUS [20]. Details of the model are beyond the scope of this paper; so only a summary will be given here. The model assumes that given an initial porosity, the voids in the porosity field will grow and coalesce as damage occurs to the material at higher stresses and strains. The model predicts the inelastic flow of the material. In Figure 2 a schematic representation of uni-axial stress-strain ($\sigma$-$\varepsilon$) behavior of plastic metal deformation following the porous metal plasticity theory is given as adapted from [20]. The porosity is $\phi$, $\sigma_{y0}$ is the porosity-free yield stress, and $\sigma_y$ is the yield stress dependent on $\phi$ which is compared to perfectly sound $\phi = 0$ material. The yield stress and behavior of the plastic curve is determined by $\phi$ and three model constants, typically determined from theory or fitting the model to experimental data. It is also possible to define a failure void fraction, where complete loss of stress bearing ability occurs in the material. This way failure of the part modeled can occur as the voids grow and coalesce at higher strains. There is much research taking place with such micromechanical models including looking at non-spherical, and higher initial void fractions up to about 20% [21].

In a recent T&O paper, Griffin [22] reported on measurements of reduction of strength properties for 8630 and 1025 steel with porosity, with ductility reduction being the most significant effect at low porosities. Experimental data for strength properties of aluminum alloys with low porosity exhibit a linear dependence that appears to be on the same order of influence as microstructural effects on the properties, as shown in Figure 3 [23]. The abscissa axes in Figures 3 A) and B) are the global average volumetric porosity for the entire specimen, and the volumetric average in the fracture region, respectively. Porosity was determined by relative density measurements. Note the porosity in the fracture region is higher than the total specimen porosity; the failures occur in the weaker parts of the material. Alloy microstructure differences are seen by comparing the hollow and filled symbols. Alloy 1 was cooled more slowly resulting in a larger average dendrite cell size, and had a lower Fe and Si content making it more ductile than Alloy 2 due to lower Si and $\beta$-Al5FeSi in the microstructure. The interplay between microstructural and porosity effects is apparent. At the low level of porosity the two compete. Alloy 1 shows much less of an effect of porosity on yield strength, but it exhibits a lower yield strength due to microstructural differences. The importance of selecting a representative method and basis for porosity evaluation is also clear, since the porosity values from Figure 3 A) to B) are quite different with A) being a volume average and B) a local porosity in the vicinity of failure, respectively.

## 2.2 Effect of High Levels of Porosity: Cellular and Foam Materials

Man-made materials in the > 70% porosity range are typically cellular or foam materials. As described primarily by Gibson and Ashby [2,17,24], physical models of these materials are developed using strut-like edges of solid material in the case of open-cell materials (for example, occurring naturally in sponges), and membrane-like walls in the case of closed-cell materials (for example a honeycomb). After constructing a model cellular structure such as those in Figure 4 [24], one can derive the stiffness and strength properties of the structure assuming wall properties of the sound material. Assuming dimensions of the edges and walls of the structure, one can relate these dimensions to the volume fraction of porosity. In terms of stiffness, the equation for elastic modulus dependent on porosity fraction for open-cell foam [24] is

$$E(\phi) = E_0 (1-\phi)^2 \qquad (4)$$

For a closed-cell foam material, it is shown [24] that the porosity fractions in the cell walls and edges need to be defined individually. Using $\varepsilon_{edge}$ to define the volume fraction of solid material in the edges of the structure, so that the volume fraction of solid in the walls is 1 - $\varepsilon_{edge}$, the elastic modulus of the closed-cell structure is [24]

$$E(\phi) = E_0 \left[ \varepsilon_{edge}{}^2 (1-\phi)^2 + (1-\varepsilon_{edge})(1-\phi) \right] \qquad (5)$$

In terms of strength, the yield strength of an open-cell foam (valid for porosity volume fraction $\phi > 0.37$) is given by

$$\sigma_y(\phi) = 0.30\, \sigma_{y0}\, (1-\phi)^{3/2} \qquad (6)$$

where $\sigma_{y0}$ of the material without porosity and $\sigma_y(\phi)$ is the yield strength at porosity volume fraction $\phi$ [24]. The yield strength of a closed-cell foam from [24] is

$$\sigma_y(\phi) = \sigma_{y0} \left[ 0.30 \left(\varepsilon_{edge}(1-\phi)\right)^{3/2} + (1-\varepsilon_{edge})(1-\phi) \right] \qquad (7)$$

Also, Gibson and Ashby [24] report that the Poisson ratio for both open- and closed-cell foams is 1/3 and not dependent on porosity amount.

The physical nature of these highly porous cellular materials is different from what is observed in porosity in steel castings. An ordered *homogeneous and isotropic* distribution of porosity, such as found in foams, is not found in steel castings. However, it is important to review some of these relations because they are often referenced in the literature, serve as limiting cases and will be referred to in some results from the literature to follow.

## 2.3 Effect of Intermediate Levels of Porosity on Static Stiffness and Strength

This porosity classification basically includes porosity levels that are large enough so that they violate the assumptions in the lowest grouping (i.e. the pores do interact), and cannot be adequately described as the regular structures found in cellular materials. In many materials that are not classifiable in the previously discussed groups, it has been experimentally observed, and demonstrated through theoretical and computational modeling, that there is a *critical porosity fraction.* At porosity levels above this critical value there is no longer interconnected solid throughout the volume of material. At this point the material looses all load carrying capability, and the elastic modulus is zero.

Rice [25,26] has determined property-porosity relationships for geometric stackings of solid spheres with interstitial pores, or alternatively spherical pores with solid interstitial spaces. His fundamental assumption is that the ratio of the effective porous material properties to the sound/solid material property is directly proportional to the ratio of the minimum solid contact area to total cross-section area in a porous structure. He argues that cellular materials can be shown to be special cases of such stackings. In Figure 5 two stacking arrangements are shown, a cubic array Figure 5 A) and an orthorhombic array Figure 5 B). The areas of contact (assuming a packing of uniform-sized solid spheres) for the porosity level of the packing is indicated by the hatched areas. Note that if the packing is porosity-free, the two cases result in grain shapes of a

cube and hexagon in Figures 5 A) and B), respectively. For a given porosity level and packing of uniform-sized spheres, he develops the concept of a minimum solid area (MSA) fraction of contact for the porous structure that can be used to predict the material properties related to stress (elastic moduli and strength) or flux (thermal or electrical conductivity). In Figure 6, Rice shows [13] there exists a critical porosity fraction $\phi_0$ beyond which the minimum solid area fraction of contact in the packing asymptotically approaches 0. For the packings shown in Figure 6, $\phi_0$ varies between 0.26 and 1.0. Note that the packings of solid spheres, that might be used to approximate sintered metals, have much lower $\phi_0$ than packings for spherical pores, which would be similar to a cellular material. If the curves are redrawn by normalizing the porosity fraction with the critical porosity fraction ($\phi/\phi_0$ as indicated by the red legend and red hatched region in the plot), Rice demonstrates that all the packing curves fall into the red hatched region in Figure 6. This emphasizes the importance of $\phi_0$ as a parameter, and provides a physical basis for the functional dependence of material properties, for example elastic modulus, on porosity of the form

$$E(\phi) = E_0 \left(1 - \frac{\phi}{\phi_0}\right)^n \tag{8}$$

where n is a power exponent that has been found to vary between 0.5 and 4 [13]. Using elastic modulus as our property of interest, consider the plot in Figure 7 from [13]. Bert [10] first suggested that the elastic modulus depended on porosity according to Equation (8) based on empirical observation of experimental data. He also hypothesized that the exponent n was dependent on $\phi_0$ as well, having the form

$$n = K_t \, \phi_0 \tag{9}$$

where $K_t$ is a stress concentration factor related to type and characteristics of the porosity. Rice presents the plot shown in Figure 8 that supports the hypothesis that n is correlated with $\phi_0$; n increasing with increasing $\phi_0$. The data in Figure 8 comprises experimental results for metals, ceramics, and the computer generated porous structures analyzed in [27].

These computer generated structures, the star data points in Figure 8, were investigated by Roberts and Garboczi [27]. They developed computer generated random porous structures having porosity fractions of 0.1, 0.2, 0.3, 0.4 and 0.5 made up of three fundamental geometries; overlapping solid spheres, overlapping spherical pores and overlapping ellipsoidal pores. Example volumes of the structures analyzed are given in Figure 9. In generating the structure, the geometric bodies were randomly sized and positioned to achieve the desired porosity fraction. In the case of the ellipsoids, they were randomly oriented. In their study, Roberts and Garboczi [27] define the solid elastic modulus $E_0$ and the Poisson ratio $\nu_s$ for the solid in the structure. The solid structure is then meshed and analyzed using finite element analysis. Poisson ratios of the solid $\nu_s$ were varied from -0.1 to 0.4 to determine the dependency of the resulting Poisson ratio $\nu$ for the porous structure as a function of porosity, and to determine whether there was any variation in the E versus $\phi$ curves with solid Poisson ratio. The elastic modulus versus porosity plot for their results is given in Figure 10 [27], where their results were fitted to Equation (8) giving the n and $\phi_0$ for each structure. Note that results for solid Poisson ratios $\nu_s$ from -0.1 to 0.4 are plotted in Figure 10 at each $\phi$ value and are seen to be nearly identical. The E versus $\phi$ curves were not influenced by the solid Poisson ratio. Assuming the solid Poisson

ratio $\nu_s$, Roberts and Garboczi [27] determined relationships between Poisson ratio $\nu$ and porosity $\phi$ for the structures. The results for the overlapping solid sphere structure are shown in Figure 11, and they approach an asymptotic limit with increasing porosity. They fitted the results for the three structures to a linear relationship of Poisson ratio versus porosity

$$\nu(\phi) = \nu_s + \frac{\phi}{\phi_\infty}\left(\nu_\infty - \nu_s\right) \qquad (10)$$

where there are three parameters; the Poisson ratio for the solid $\nu_s$, the asymptotic limiting value of Poisson ratio $\nu_\infty$, and the porosity value corresponding to the asymptotic limit $\phi_\infty$. The results in Figure 11 are typical of the results for the other structures. The asymptotic parameters for use in Equation (10) are: 1) for the overlapping solid spheres $\nu_\infty = 0.14$ and $\phi_\infty = 0.472$, 2) for the overlapping spherical pores $\nu_\infty = 0.221$ and $\phi_\infty = 0.840$, and 3) for the overlapping ellipsoidal pores $\nu_\infty = 0.166$ and $\phi_\infty = 0.604$. Similar asymptotic results for $\nu$ versus $\phi$ are obtained using the generalized method of cells [11] and continuum mechanics [28].

The generalized method of cells (GMC) has been used to predict the elastic properties of aluminum oxide ($Al_2O_3$) and the inelastic non-linear response of the intermetallic nickel compound IC-50 [11]. The method models a unit cell as a representative volume of a periodic structure, and discretizes and solves the micromechanical equations for a visco-plastic material. This method provides an excellent tool for examining directly the effect of pore geometry on elastic modulus and strength. Herakovich and Baxter consider the four idealized pore shapes shown in Figure 12; cylinder, cube, sphere, and cross shaped pores. The results for elastic modulus of $Al_2O_3$ in Figure 13 are compared with the experimental data from [16]. The cylindrical pore shows almost a perfect linear rule of mixtures Equation (1) behavior, and the cross shows the most degradation in E. The spherical pore has the second most reduction in E, and the third most reduced is the cube. The experimental data [16] shows good agreement with the spherical pore and the cross-shaped pore. The porosity level is increased while maintaining each pore shape until the "b" dimension (shown in Figure 12) in each unit cell approaches 0; at this point the pores would touch the neighboring periodic cell's pore and a critical pore fraction is reached. Additional results are not possible beyond this pore fraction. The critical pore fraction for the spherical pore is for example 0.5236; which is the ratio of volumes of a sphere of radius R to a cube of radius 2R. This study clearly shows that pore geometry can be as important as pore volume fraction to E. As shown in Figure 13, at the same porosity volume fraction the elastic modulus of the porous material can vary by up to two times for different pore shapes. The effect of pore geometry and porosity level on non-linear (elastic-plastic) tensile response is given by in Figures 14 and 15 for the intermetallic nickel compound IC-50 (11.3 wt% Al, 0.6 wt% Zr, 0.02 wt% B, balance Ni) [11]. In Figure 14, the effect of pore shape on the tensile curves of material with a porosity fraction of 0.2 is shown. As expected from the results of E, the cross has the most reduced load resistance capability, followed by the sphere, then cube, and then the cylinder. The differences in E are apparent from the slopes of the elastic portion of Figure 14 taken from [11], and note that the yield strengths are also affected and reduced by pore shape alone. Figure 15 is provided from [11] to demonstrate the effect of porosity fraction for a given pore shape; the spherical pore. Porosity level is clearly affecting both stiffness and strength in Figure 15.

Compared to ceramics, there is less experimental data in the literature for stiffness and strength behavior of metals with well-characterized porosity. Most of the literature in porous

metals examines sintered materials [9, 29]. Since sintered materials are relatively homogeneous, they can be well-characterized; by a representative porosity fraction determined from relative density measurement, and microscopy can be used to determine pore size distributions, etc.

Zhang and Wang [9] give an experimental study of the elastic-plastic properties of porous sintered copper made from 5 and 45 μm copper powder. The two powder sizes result in two solid structures with differing microvoid regions between the sintered powder grains. The macro-porosity levels (5.9% to 55.5%) were produced by mixing varying amounts of 600 μm polymethylmethacrylate (PMMA) polymeric powder into the copper powder prior to sintering. These particles vaporized during sintering resulting in about 200-500 μm pores. Representative stress-strain curves for porous sintered 5 μm copper powder with 5.9% to 55.5% porosity in compression are shown in Figure 16 from [9]. Note the reduced elastic modulus from the slopes of the initial part of the curves in Figure 16, and the yielding behavior, as functions of porosity. As shown in Figure 17 A) adapted from [9], the relative elastic modulus ($E/E_0$) for their data versus porosity is compared with the Gibson-Ashby model for closed-cell materials given in Equation (5) (with $\varepsilon_{edge} = 0.8$), and porous titanium data [28]. Note that their data has a very dramatic drop-off in $E/E_0$, $E/E_0$ is less than 0.1 even at about 5% porosity. This dramatic drop may be due to microporosity in their "sound" material due to the spaces between the copper powder grains, since their $E_0$ was based on sound copper. A more fair comparison would have been to use their 5.9% porosity specimen data for the "sound" comparison since it had no 600 μm PMMA powder added. Nevertheless, the elastic modulus does not appear to be effected by the different sized powder grains. Since elastic modulus is not believed to be influenced by grain size in porosity-free metals, this is not surprising. From Figure 17 A) the critical porosity fraction for porous copper appears to be around 30%, where $E/E_0$ is very small. For the porous titanium, the smallest porosity level is about 35%, and for that value $E/E_0$ is 0.1; more data in the low porosity range would be desirable. The closed-cell material relation, Equation (5), does not show the dramatic drop in relative elastic modulus seen in the experimental data, and the Zhang and Wang [9] believe this is due to the metal having microporosity. Figure 17 B) shows the 0.2% compressive yield strength for the two sizes of copper powder versus porosity and comparison with Equation (7) for closed-cell foam. Two important observations are that the yield strength is linearly reduced with porosity percentage, and that the yield strength is dependent on the powder size from the two distinct distributions of microporosity between the metal grains. The smaller grains (5 μm powder) have finer microporosity and higher yield strength.

## 2.4 Past Work and Background for the Present Study

At the 2004 SFSA T&O Conference the present authors described a method of quantitative analysis of radiographs to determine porosity in the cross-sections of fatigue test specimens [6]. We subsequently developed that technique into a method of performing x-ray tomography, or three-dimensional reconstruction of porosity in the specimens. Examples of porosity distributions generated by the technique are shown for two specimens in Figure 18. In Figure 18 actual cut surfaces of specimens are compared to the porosity distributions on the same surfaces from the tomography results. It should be apparent that the porosity in these 8630 steel specimens, like the porosity detectable by radiography in most steel castings, is not homogenous or uniform throughout an entire section. This poses a dilemma in generating material property data that is representative of a given porosity level such as that discussed in sections 2.1 to 2.3 of this paper.

Consider that when the measured elastic modulus from the test data [6] is plotted versus the volumetric average porosity in the test section determined from the tomography as shown in Figure 19, the elastic modulus varies by over a factor of 2, from 162 to 77 GPa (or a relative $E/E_0$ from 0.78 to 0.37 based on $E_0$ = 207 GPa), and the variation in average porosity is about 15% to 25%. There appears to be no dependency on average porosity. Any average porosity is likely to have any value of elastic modulus, because **the modulus depends on how the porosity is distributed**, per the discussion of Figure 10. In [6] we *did* show a good correlation between the maximum section porosity along the gage section length and the elastic modulus as shown in Figure 20. The maximum section porosity should be related to the minimum section area, and this seems to be in agreement with the minimum solid area concepts proposed by Rice [25,26]. Unfortunately, the correlation shown by the data in Figure 20 could not be used as an E versus $\phi$ relation. It emphasizes that the porosity distribution is as important as the amount of porosity, and the maximum section porosity is more closely related to how the porosity is distributed in this case.

The fundamental goal of the present work is to determine an E versus $\phi$ relationship that could be applied to any distribution of porosity giving agreement between measured and predicted elastic modulus. The test specimens from [6] were used for this study with x-ray tomography used to determine the specimen porosity distribution. This porosity distribution was imported into finite element simulations where the material properties were dependent on the porosity.

## 3. Analytical Procedure

Using radiographs of the test specimens, the porosity $\phi$ distributions in the specimens are determined based on computed tomography. The porosity distribution is then mapped to the nodes of a finite element stress-strain analysis (FEA) mesh. Figures 21 and 22 are provided to show for one specimen the output of a porosity distribution from tomography, and the distribution resulting from mapping the tomography results onto the finite element mesh, respectively. Here the tomography results are determined on a 3-D grid determined by the 1200 dpi resolution from the digital radiographs. The FEA mesh is approximately 20 to 50 times coarser. Therefore one issue needing exploration is how the 3-D interpolation of the tomography $\phi$ field onto the FEA mesh field influences results; and a second important issue is how the coarseness of the FEA mesh influences results.

Once the interpolation is performed, the material properties in the FEA stress analysis are made dependent on the porosity field. An elastic modulus versus porosity relationship was used to model the effect of porosity on stiffness; based on the literature survey Equation (8) was used. Determining the relationship of E versus $\phi$ which provides the best agreement between predicted and measured strain over all test specimens was the primary goal. Achieving this goal involved iteratively running FEA simulations using ABAQUS [20] on all specimens for their test conditions, and changing the E versus $\phi$ data until the best relationship is determined for all specimens. Predicted strain was determined from the FEA simulations using the relative displacements at the locations surface of the specimen FEA model where the extensometer was placed in testing. This location was 6 mm above and 6 mm below the center of the specimen gage section. In the case of Poisson ratio, this was not measured, so we cannot determine the best relation to use. In this study it was made variable according to Equation (10) using the

overlapping solid sphere result from [12] with $\nu_\infty = 0.14$, $\phi_\infty = 0.472$ and $\nu_s = 0.3$. There is evidence that Poisson ratio does not have a large effect of the effective elastic modulus as discussed regarding Figure 10 [12]. Because there was not significant plasticity detected during testing of the specimens, and plastic behavior such as yield strength was not measured as a function of porosity, plastic effects were ignored in the FEA simulations used to develop the best E versus $\phi$ relationship. It is recommended that plasticity and strength behavior be investigated in future work.

# 4. Results and Discussion

## 4.1 Interpolation of Specimen Porosity Field

Two methods of performing the interpolation of the tomography porosity distribution results to the finite element mesh were tested as shown in Figure 23. One method used a 3-D quadratic interpolation scheme to map the porosity in the tomography data to the FEA mesh, which is shown in Figure 23 A). The second method took the average of a cubic volume of tomography porosity data centered at a node with the side dimension of the cube determined by the node spacing. The averaged cubic volume method shown in Figure 23 B) resulted in a more diffuse representation of the porosity. The differences between the two shown in Figure 23 are subtle. The FEA simulation results for the two porosity interpolation methods were compared on several meshes to look at the effects of grid coarseness, and determine the best combination of interpolation and grid to use in the simulation runs to follow. Examples of three of the FEA meshes used in the grid study (node spacings of 1, 0.5 and 0.3 mm) are shown in Figure 24. The specimen test/gage section diameter was 5 mm.

Grid studies using porosity distributions from two specimens were compared. The specimens were chosen because they were tested at the same stress level (96 MPa or 13.9 ksi) yet had different levels of porosity, as seen in Figures 25 A) and B). The ram end (or grip) displacement was selected as the variable to monitor for the grid studies. From Figure 25 C), the ram end displacement of the more porous specimen, E5, is about 33% larger than the less porous specimen C2. Specimen C2 does not appear to show much of an effect of either grid spacing or interpolation method. Specimen E5 ram end displacement shows that the average volumetric interpolation monotonically converges with finer grids, while the quadratic interpolation displacements do not. The displacement for 1 mm spacing is farther away from the finer mesh values, and the 2 mm mesh is closer to the finer meshes. This result points out a drawback in the quadratic interpolation scheme; on coarser meshes it is more influenced by values near the node than desirable, and results can oscillate. However, it was decided to use the quadratic interpolation scheme on a fine enough mesh, to capture as much of the details of the porosity as possible. Either interpolation method would have worked well on the 0.5 mm mesh selected for the simulations used to determine the best E versus $\phi$ relationship.

## 4.2 Effect of Porosity on Elastic Modulus

Specimen E5 was chosen as a starting point for the ABAQUS FEA simulations to develop the E versus $\phi$ relationship that would give the best agreement with the measurements. This specimen had the most severe porosity and degraded E. Comparison between measured and predicted strain would be used to determine the best relation. The non-uniform porosity for

specimen E5 is shown in Figure 26 A). If the elastic modulus is made a function of porosity using Equation (8), the predicted stress-strain fields have variations throughout the porous region in the specimen gage section caused by the non-uniform stiffness. The stress and strain fields for a simulation using n = 2.5 and $\phi_0$ = 0.5 in Equation (8) are shown in Figure 26 B) and 26 C), respectively. The nominal sound gage section stress for this test was 96 MPa.

The strain measurements were made using an extensometer centered in the gage section with knife edges positioned to measure displacements at ±6 mm about the gage section center. To compare with these measurements, axial displacements at ±6 mm about the center of the gage section on the surface of the ABAQUS FEA mesh were used to determine the predicted strain. As can be seen in Figure 27 for specimen E5, the strain variations at the surface of the specimen are predicted to vary from 200 to 600 microstrain. Unfortunately, the testing did not measure these variations in strain at the surface, and the circumferential orientation of the gage was not recorded. It is assumed that the strain measured was an average strain. To compare with the measured strain, the predicted strain is determined from the simulated displacements at all node circumferential positions, 12 mm apart, centered on the gage section. A strain is determined from these values by averaging, and a 95% confidence interval is determined to provide an indication of uncertainty for this average.

Results of strain predictions using Equation (8) with $\phi_0$ = 1.0 and variable n for Specimen E5 are compared with the measured strain in Figure 28. Here the range of n (1 to 5) was selected to cover the range of values from the literature presented in Figure 8. Note that as n increases, E is reduced progressively. Also, the average predicted strain increases along with the variation in strain reflected by the confidence interval. When n = 1 (the linear relation), the strain is under predicted by about 50% and only as n is increased to 5 (a very high value, outside the range of data in the literature, Figure 8) does it approach the measured strain. Here the critical porosity is not considered, $\phi_0$ = 1.0. For $\phi_0$ = 1.0, all specimens simulated showed a greatly under-predicted strain. This is a strong indication that steel with porosity exhibits a critical porosity fraction $\phi_0$ much less than 1.0.

Taking guidance from the results in Figure 10 [12], the effect of critical porosity fraction $\phi_0$ was investigated with a baseline exponent of n = 2.25 using the elastic modulus versus porosity relation Equation (8). Five specimens were chosen because they encompassed the full range of porosity levels and nominal test stresses. The results are shown in Figure 29 with critical porosity fractions $\phi_0$ = 1.0, 0.75, and 0.5 used to generate variable stiffness properties in the FEA simulations. For each specimen, the predicted strain increases progressively as $\phi_0$ decreases; this is indicated in Figure 29 for specimen E5 at the far right in the plot. The applied nominal stress level is also indicated for each specimen in Figure 29. Note that specimen C8 was tested at the highest stress level, 126 MPa, but is only in the middle strain range of the specimens shown here. The predicted strain of specimen C8 is also not influenced much by the different critical porosity fractions $\phi_0$ because it is one of the more sound specimens tested. Specimen D4 is also relatively sound and its predicted strain is uninfluenced by changing $\phi_0$. The results in Figure 29 indicate that; 1) $\phi_0$ has a non-linear effect on the strain prediction and 2) that $\phi_0$ = 0.5 provides the best agreement for the range of specimens analyzed in Figure 29. The non-linear behavior of the specimens in response to changing $\phi_0$ is driven by the porosity distribution in the specimens.

The best fit for the parameters n and $\phi_0$ in the elastic modulus versus porosity relation (Equation (8)) was achieved by minimizing the error between the predicted and measured strain for all specimens available. This was accomplished by a painstaking trial and error procedure: 1) generating the elastic modulus versus porosity data according to the Eq. (8) for a given n and $\phi_0$, 2) importing that data in a format usable by ABAQUS, 3) running ABAQUS simulations for the applied nominal stress conditions for specimens with a porosity field and porosity dependent E and $\nu$, and 4) comparing the measured and predicted strain and determining how to change n and $\phi_0$ to get better agreement. Good agreement between the measured and predicted strain was obtained using Equation (8) with n = 2.5, and critical porosity fraction $\phi_0 = 0.5$. This is shown in Figure 30. Comparison of the n and $\phi_0$ from this work with those in Figure 8 is good. Our n value is on the upper end of the data for our $\phi_0$. However, given that the porosity distributions in our specimens is very inhomogeneous relative to the materials tested in Figure 8, the results of this study agree well with the stiffness behavior of other porous materials.

Examining the variation in elastic modulus reinforces the importance of porosity distribution on material behavior. For example consider Figure 31, two specimens (D5 and H7) have nearly identical average porosity levels in the gage section (porosity fractions of 0.146 and 0.144) and the testing gave very different elastic moduli (87 and 142 GPa, respectively). Examining the predicted and measured strain, there is not a great difference between the strains, and one specimen was tested at a nominal stress level of 53 and the other at 96 MPa. The porosity in specimen D5 appears to be severe in one slice along the axis as shown in Figure 31, and this feature of distribution of porosity greatly affects the resulting behavior. The results of the predicted strain were converted to a predicted elastic modulus by using the test's nominal stress so that

$$E_{predicted} = \frac{\sigma_{nominal}}{\varepsilon_{predicted}} \qquad (11)$$

where $\sigma_{nominal}$ is the applied test stress based on the specimen cross sectional area and $\varepsilon_{predicted}$ is the predicted strain. The predicted and measure elastic moduli are plotted in Figure 32, and the agreement still appears good. Uncertainty intervals are not plotted in Figure 32, because they tend to obscure the data. By modeling the effect of the porosity distribution in the FEA simulations, the material behavior is accurately predicted since with the uncertainty interval all data are within the bands of ±10% agreement. The effect of differences in the distribution of porosity in specimens like those shown in Figure 31 can be predicted by the method presented here.

## Conclusions and Recommendations

It has been demonstrated that steel exhibits a critical porosity level that is substantially less than a porosity fraction of 1.0. When porosity exceeds this level the material essentially looses all stiffness or load carrying capability. It has also been shown that the elastic modulus decreases non-linearly. The equation found to give good agreement between measured and predicted elastic modulus is

$$E(\phi) = E_0 \left(1 - \frac{\phi}{0.5}\right)^{2.5}$$

A thorough review of the literature on the properties of porous materials supports this finding. The stiffness behavior of steel with porosity can be accurately modeled by incorporating the elastic modulus as a function of porosity into finite element simulations, which should result in accurate stress-strain fields for the elastic range. The result is a major advance from past work in the area because it considers a non-uniform distribution of porosity such as that found in steel castings, and demonstrates that in homogeneities due to porosity can be considered in part design.

It is recommended that future work consider investigating the elastic-plastic behavior of steel with porosity. Since the current work analyzed data in the elastic range, from fatigue tests, it is proposed that the same approach of coupling accurate tomography data to determine porosity distributions, and use porosity dependent material property data in FEA simulations to investigate and develop predictive models. Additional specimens must be produced and testing performed. If possible, the variation of strain predicted on the surface of specimens with porosity should be verified during testing. Finally, since some theoretical models of materials with porosity can be extended to a "hard" second phase (such as an inclusion), it is recommended that the approach described in this paper be applied to steel with inclusions.

## Acknowledgments

This research was undertaken as part of the *Integrated Design of Steel Castings for Service Performance* and the *Cast Part Performance in the Presence of Discontinuities* projects which are funded by the United States Department of Defense through the American Metalcasting Consortium (AMC) program. AMC is sponsored by Defense Supply Center Philadelphia (DSC, Philadelphia, PA) and the Defense Logistics Agency (DLA, Ft. Belvoir, VA). This research is also conducted under the auspices of the Steel Founders' Society of America, and through substantial in-kind support, guidance and interest from SFSA member foundries. In particular, we would like to thank Harrison Steel for several trial iterations of test specimens and the final test specimen castings, Alloy Weld Inspection Co. for their digital and film radiography of the fatigue test specimens, Southern Cast Products for their willingness to create a new test specimen casting pattern and to cast new test specimens. Any opinions, findings, conclusions, or recommendations expressed herein are those of the authors and do not necessarily reflect the views of DSC, DLA, or the SFSA and any of its members.

## References

1. Ashby, M.F., Evans, A.G., Fleck, N.A., Gibson, L.J., Hutchinson, J.W., and Wadley, H.N.G, *Metal Foams: A Design Guide* (Butterworth-Heinemann, Boston, 2000).

2. Gibson L.J., and Ashby M.F., *Cellular Solids: Structure and Properties* (2nd ed., Oxford, Pergamon Press, 1997).

3. P. Heuler, C. Berger, J. Motz, "Fatigue Behaviour of Steel Castings Containing Near-Surface Defects", *Fatigue & Fracture of Engineering Materials & Structures*, 1992, **16(1)**, pp. 115-136.

4. Sigl, K.M., Hardin, R., Stephens, R.I., and Beckermann, C., "Fatigue of 8630 Cast Steel in the Presence of Shrinkage Porosity," in Proceedings of the 57th Technical and Operating Conference, SFSA, Chicago (2003).

5. K.M. Sigl, R. Hardin, R.I. Stephens, and C. Beckermann, "Fatigue of 8630 Cast Steel in the Presence of Porosity," *International Journal of Cast Metals Research*, 2004, 17(3), pp. 130-146.

6. Hardin, R. and Beckermann, C., "Effect of Porosity on Mechanical Properties of 8630 Cast Steel," in Proceedings of the 58th Technical and Operating Conference, SFSA, Chicago (2004).

7. Horstemeyer, M.F., "Mapping Failure by Microstructure-Property Modeling", *Journal of Metals*, 2001, Sept., pp. 24-27.

8. Horstemeyer, M.F. , Osborne, R.J., and Penrod, D.E., "Microstructure-Property Analysis and Optimization of Control Arm", *AFS Trans.*, 2002, 02-036, pp. 1-18.

9. Zhang E. and Wang B., "On the Compressive Behavior of Sintered Porous Coppers with Low to Medium Porosities – Part I: Experimental Study," *Int. Journal of Mechanical Sciences*, 2005, 47, pp. 744-756.

10. Bert, C.W., "Prediction of Elastic Moduli of Solids with Oriented Porosity," *Journal of Materials Science*, 1985, 20, pp. 2220-2224.

11. Herakovich, C.T., and Baxter, S.C., "Influence of Pore Geometry on the Effective Response of Porous Media," *Journal of Materials Science*, 1999, 34, pp.1595-1609.

12. Roberts, A.P., and Garboczi, E.J., "Elastic Properties of Model Porous Ceramics," *J. Am. Ceram. Soc.*, 2000, 83(12), pp. 3041-3048.

13. Rice, R. W., "Use of Normalized Porosity in Models for the Porosity Dependence of Mechanical Properties", *Journal of Materials Science*, 2005, 40, pp. 983-989

14. Dewey, J.M., "The Elastic Constants of Materials Loaded with Non-rigid Fillers," *Journal of Applied Physics*, 1947, 18, pp. 578-581.

15. Sumitomo, T, Caceres, C.H., and Veidt, M., "The Elastic Modulus of Cast Mg-Al-Zn Alloys," *Journal of Light Metals*, 2002, 2, pp. 49-56.

16. Coble, R.L. and Kingery, W.D., "Effect of Porosity on Physical Properties of Alumina," *J. Am. Ceram. Soc.*, 1956, 39(11), pp. 377–385.

17. Maiti, S.K., Gibson, L.J. and Ashby, M.F., "Deformation and Energy Absorption Diagrams for Cellular Solids," *Acta Metallurgica*, 1984, pp. 1963-1975.

18. Gurson, A.L., “Continuum Theory of Ductile Rupture by Void Nucleation and Growth: Part I — Yield Criteria and Flow Rules for Porous Ductile Materials,” *Journal of Engineering Materials and Technology*, 1977, 99, pp. 2–15.

19. Tvergaard, V., “Influence of Voids on Shear Band Instabilities under Plane Strain Condition,” *International Journal of Fracture Mechanics*, 1981, 17, pp. 389–407.

20. Hibbit, Karlsson & Sorensen, Inc., *ABAQUS Theory Manual*, Version 6.5, 2004, section 4.3.6

21. Lassance, D, Scheyvaerts, F. and Pardoen, T., “Growth and Coalescence of Penny-shaped Voids in Metallic Alloys,” *Engineering Fracture Mechanics*, 2006, 73, pp. 1009-1034.

22. Griffin, J. A., “Effect of Porosity on the tensile and Charpy Properties of 8630 Cast Steel,” in Proceedings of the 57th Technical and Operating Conference, SFSA, Chicago (2003).

23. Mugica, G., Tovio, D., Cuyas, J., and Gonzalez, A., “Effect of Porosity on Tensile Properties of Low Ductility Aluminum Alloys”, *Materials Research*, 2004, 7(2), pp. 221-229.

24. Gibson, L.J. and Ashby, M.F., “The Mechanics of Three-dimensional Cellular Materials,” *Proc. R. Soc. Lond. A*, 1982, 382, pp. 43-59.

25. Rice, R.W., “Evaluating Porosity Parameters for Porosity-Property Relations,” *J. Am. Ceram. Soc.*, 1995, 76 [7], pp. 1801-1808.

26. Rice, R.W., “Evaluation and Extension of Physical Property–Porosity Models Based on Minimum Solid Area,” *J. Mater. Sci.*, 1996, 31, pp. 102–118.

27. Roberts, A.P., and Garboczi, E.J., "Elastic Properties of Model Porous Ceramics," *J. Am. Ceram. Soc.*, 2000, 83(12). pp. 3041-3048.

28. Ramakrishnan, N. and Arunachalam, V.S., “Effective Elastic Moduli of Ceramic Materials,” *J. Am. Ceram. Soc.*, 1993, 76(11), pp. 2745–2752.

29. Wen C.E., “Processing and Mechanical Properties of Autogenous Titanium Implant Materials,” *Journal of Materials Science-Materials in Medicine*, 2002, 13, pp. 397–401.

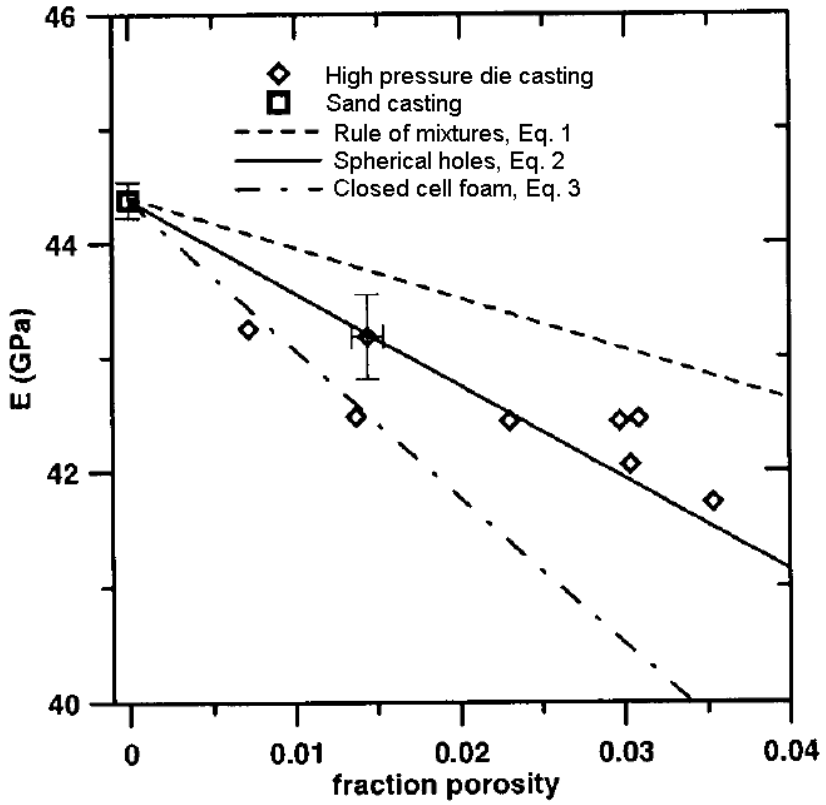


Figure 1 Elastic modulus versus porosity for the Mg-Al-Zn alloy AZ91 [15], measured sand and high pressure die cast specimen data are compared with Eqs. 1, 2 and 3.

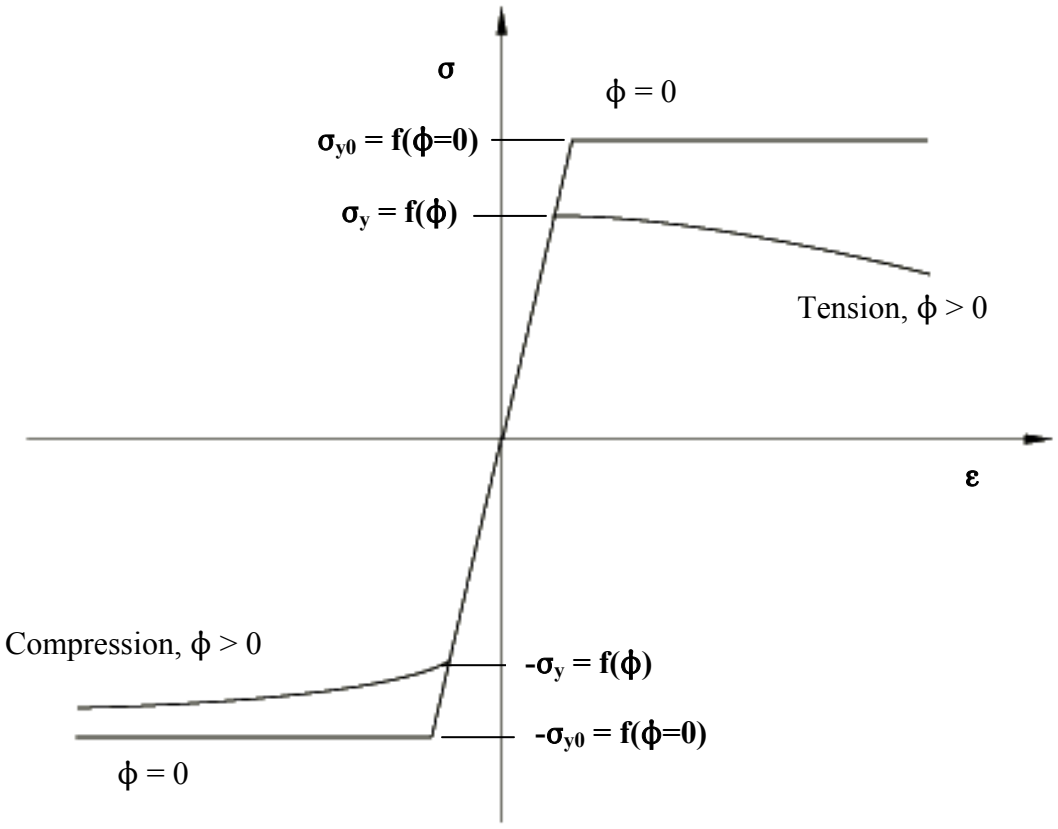


Figure 2 Schematic representation of uni-axial stress-strain (σ-ε) behavior of plastic metal deformation following the porous metal plasticity theory as adapted from [20]. Porosity is $\phi$, $\sigma_{y0}$ is the porosity-free yield stress, and $\sigma_y$ is the yield stress dependent on $\phi$.

| Chemical compositions of 380 aluminum alloys. | | | | | | | | |
|---|---|---|---|---|---|---|---|---|
| | Composition (% in weight) | | | | | | | |
| | Si | Fe | Mg | Mn | Cu | Zn | Ni | Sn |
| Alloy 1 | 8.21 | 0.75 | 0.01 | 0.32 | 3.47 | 1.38 | 0.02 | 0.02 |
| Alloy 2 | 9.17 | 0.99 | 0.02 | 0.30 | 3.12 | 0.78 | 0.02 | 0.02 |

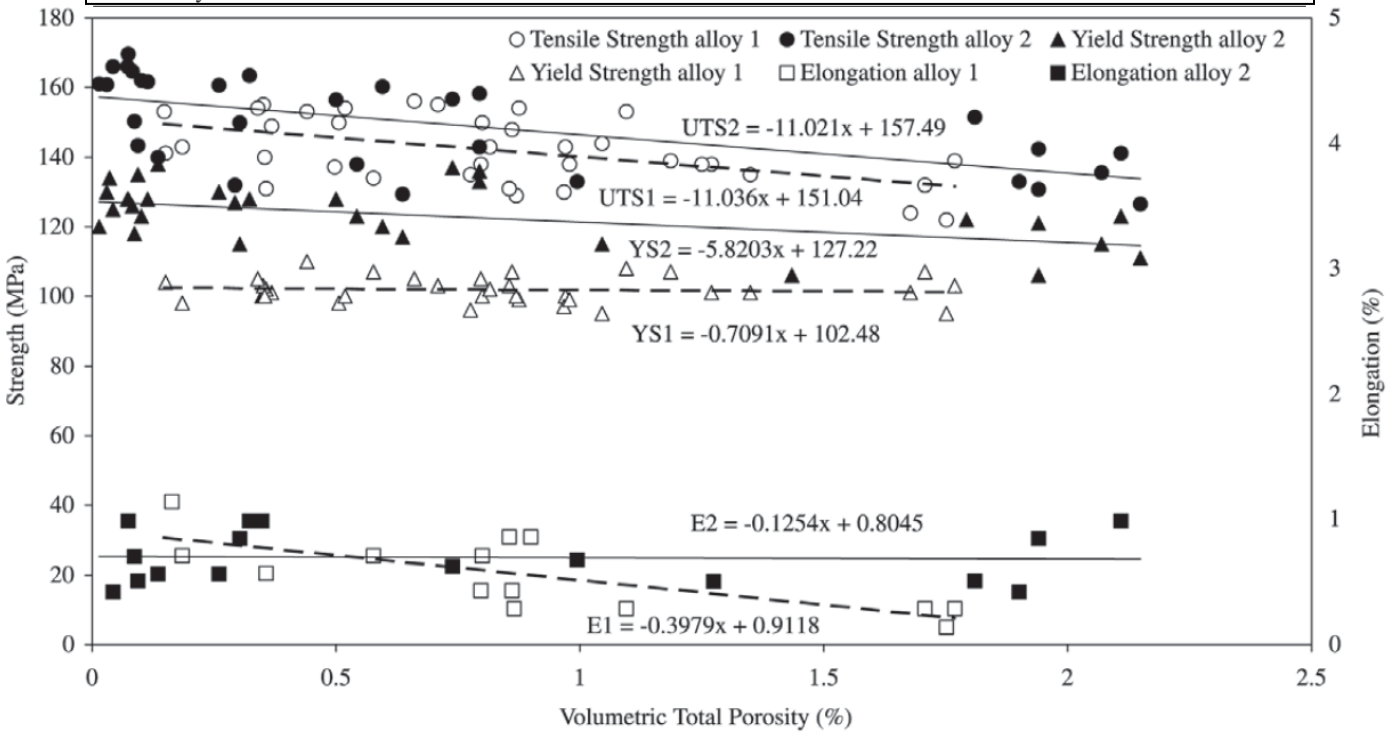


A)

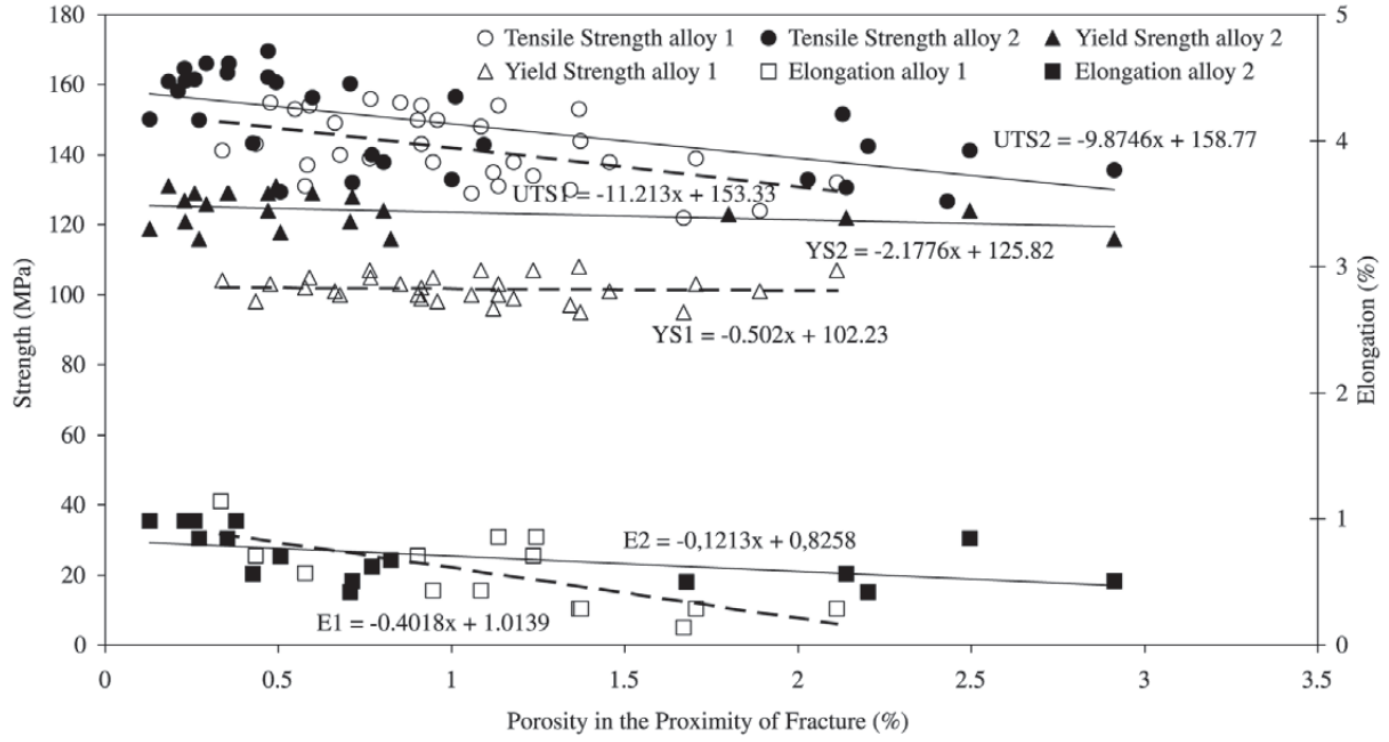


B)

Figure 3 Ultimate tensile and yield strength, and elongation for two 380 aluminum alloys whose chemistry is given above the figures [23]. A) above, versus volumetric porosity of entire specimen, B) below, versus porosity data from the proximity of the fracture.

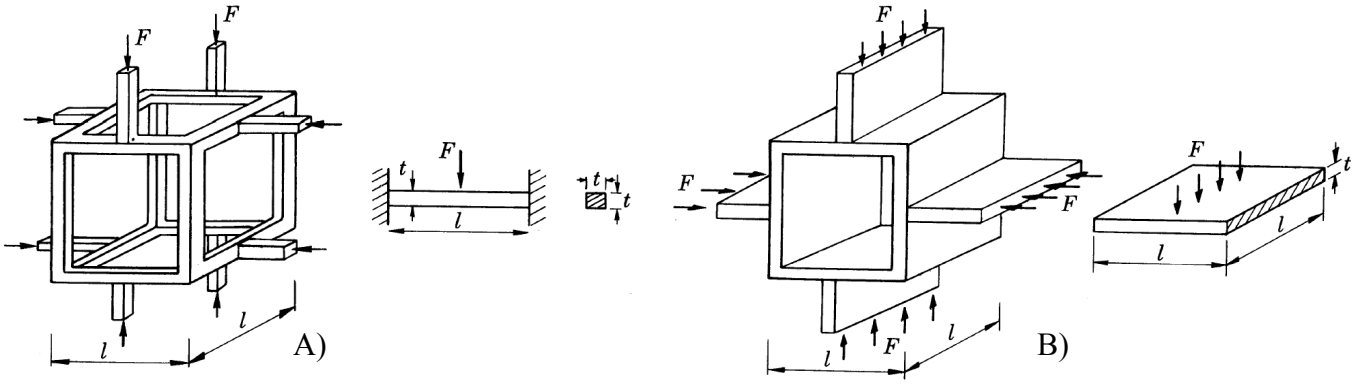


Figure 4 Examples of cubic models of porous cellular structures in compression from [17]. A) an open cellular structure, and B) a closed cellular structure.

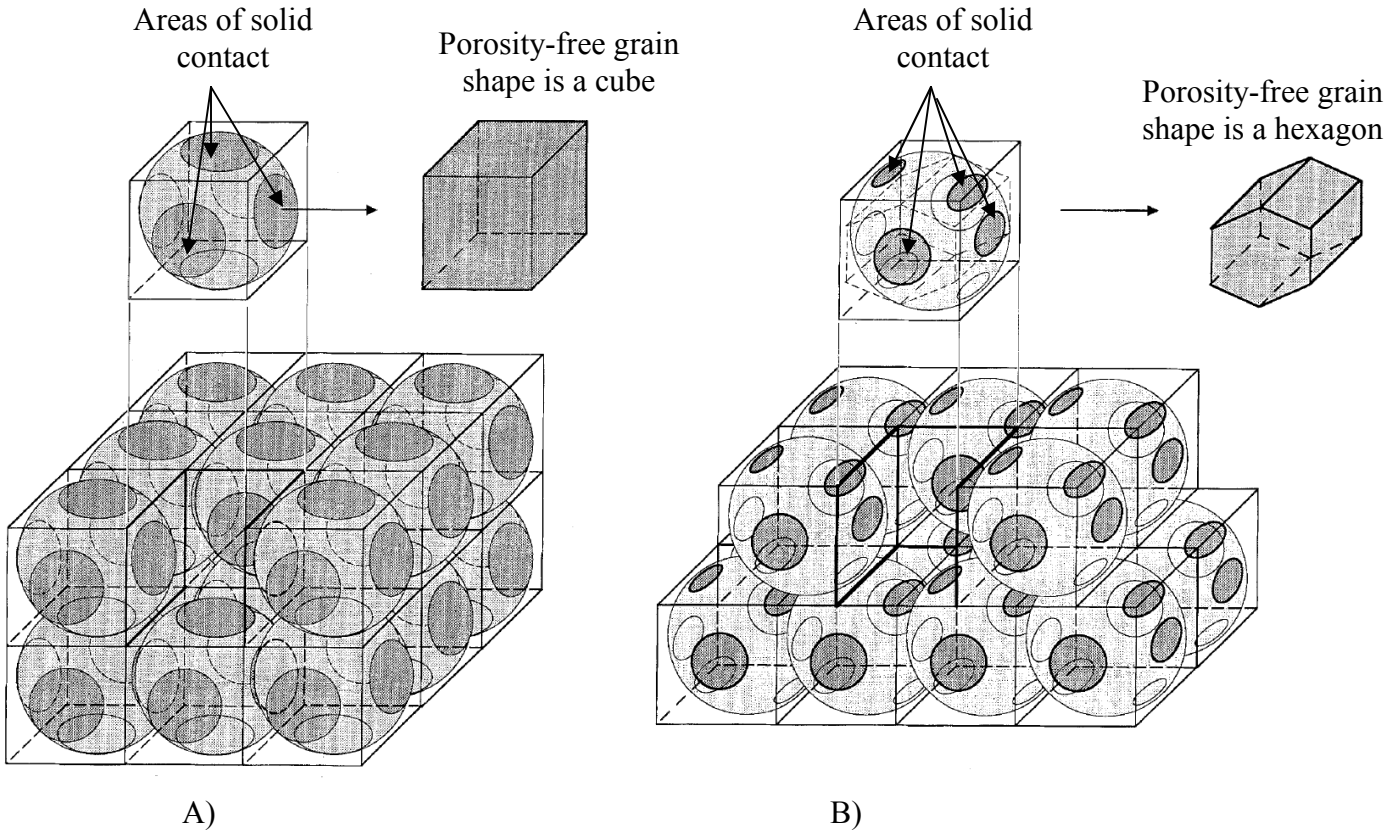


Figure 5 Examples of idealized stackings of uniformed-size solid spheres (or, alternatively, pores) in A) a cubic array, and B) an orthorhombic array from [25]. The area of solid contact is shown as hatched area, and the resulting porosity-free grain that would form in each stacking is shown upper right of each image; a cube and hexagon.

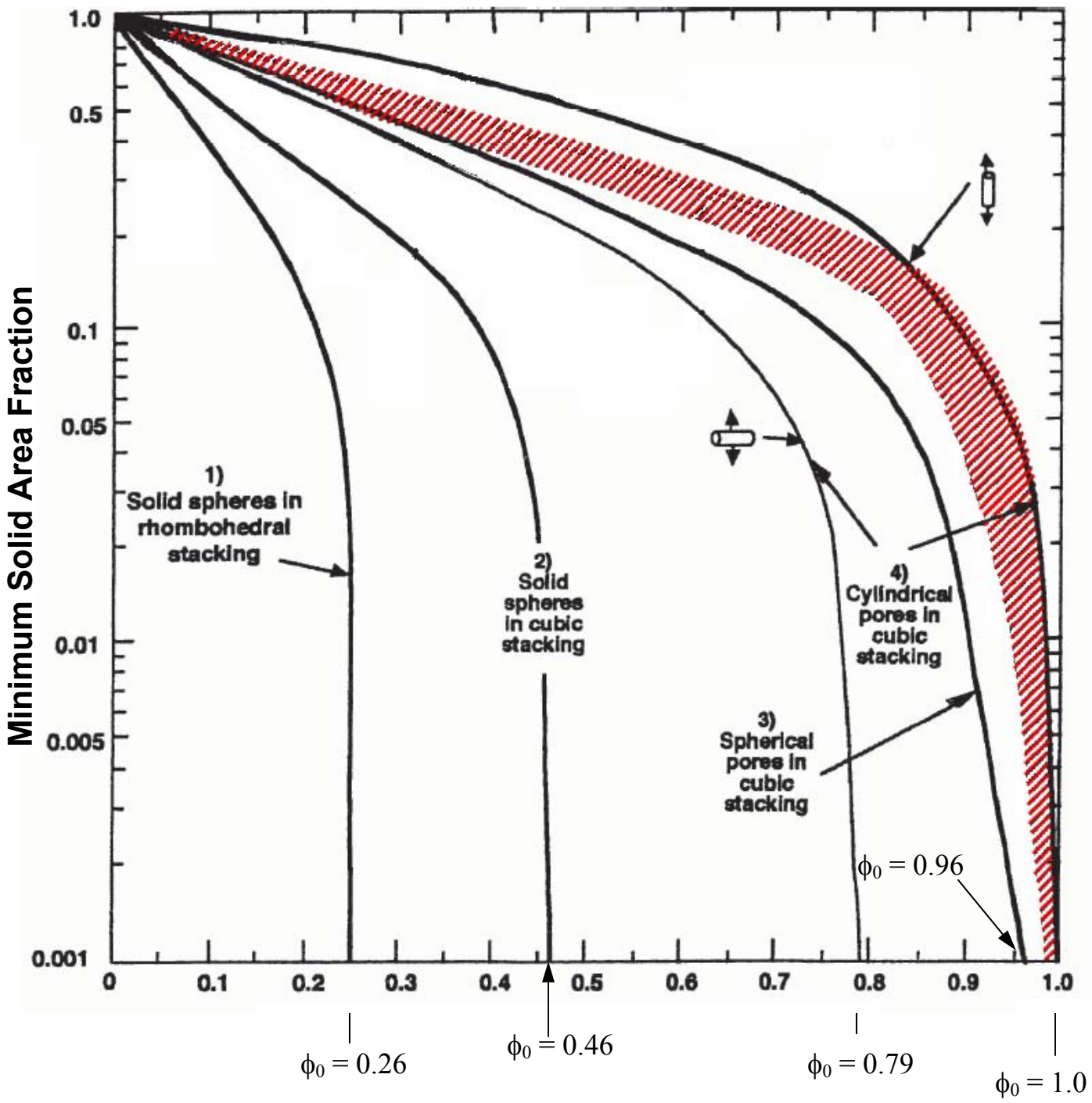


Figure 6 Results from [13] for minimum solid area fraction (MSA) of contact for packings of solid spheres, and spherical and cylindrical pores. Critical pore fraction $\phi_0$ occurs when MSA drops asymptotically. All packing curves collapse into red hatched area of plot when normalized with their respective $\phi_0$ value shown in the second axis label in red text.

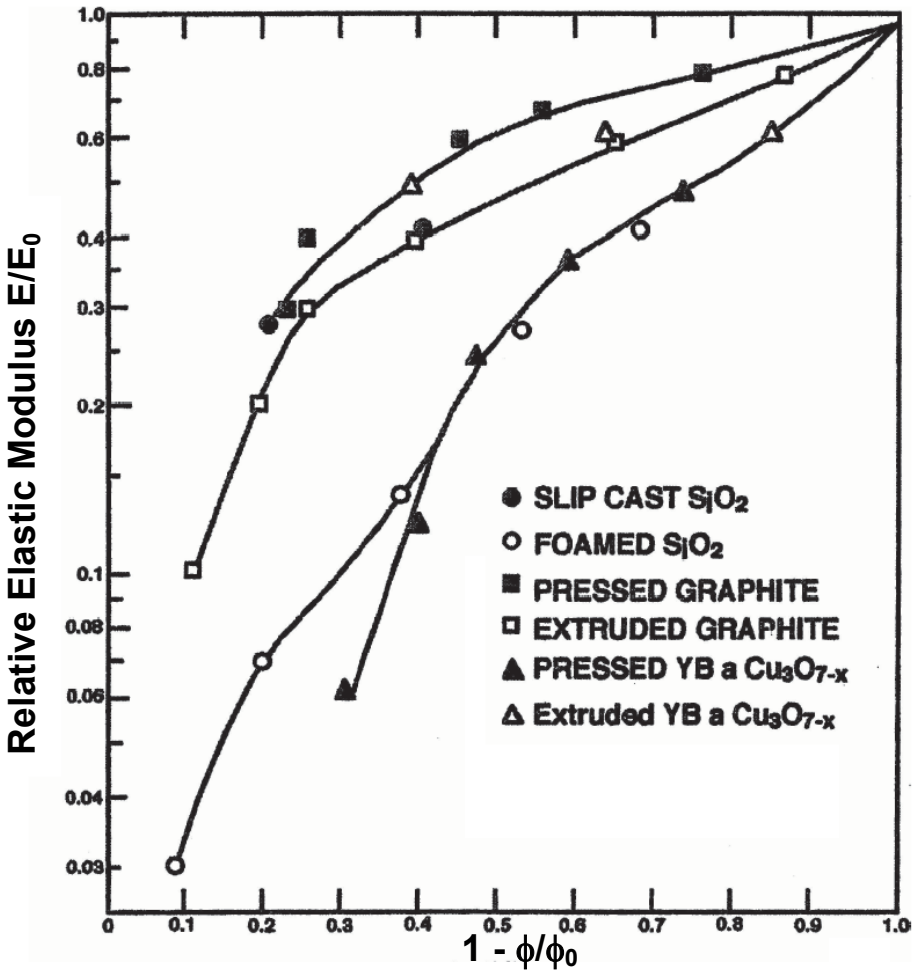


Figure 7 Relative elastic modulus $E/E_0$ versus $1-\phi/\phi_0$ for six porous material shown to follow functional form of Equation (8) according to the MSA model from [13].

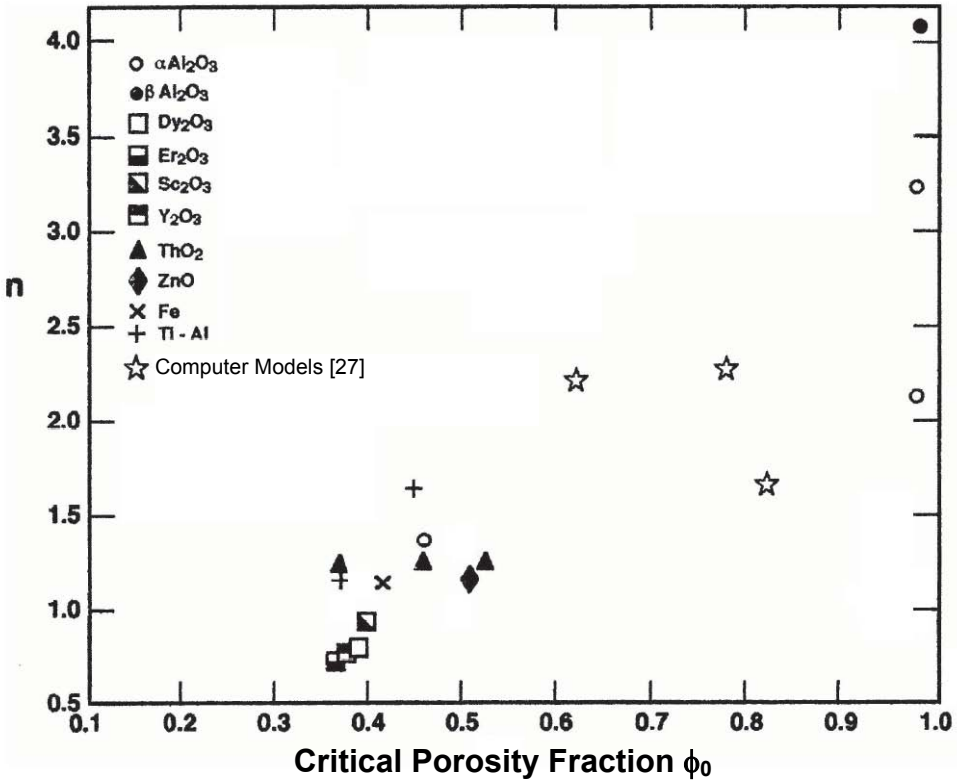


Figure 8 Exponent n from Equation (8) versus critical porosity fraction $\phi_0$ for ceramic, metal and computer generated materials shows a correlation of increasing n with $\phi_0$ [13].

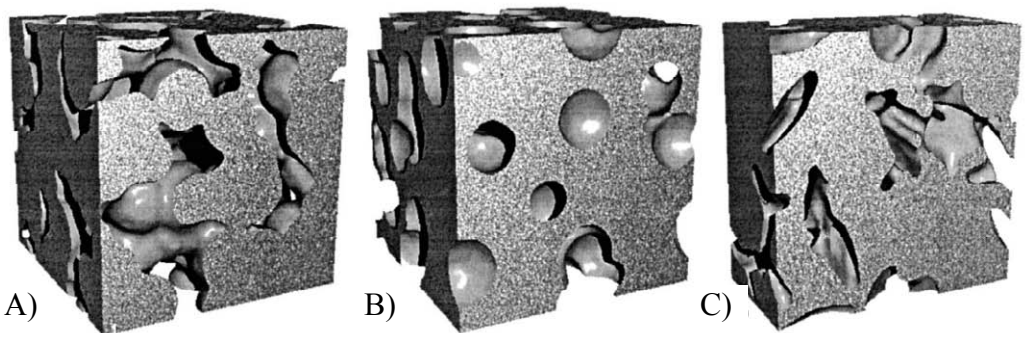


Figure 9 Representative volumes of porous structures studied by Roberts and Garboczi, taken from [27]. Volumes are computer generated random structures made up of A) overlapping solid spheres, B) overlapping spherical pores and C) overlapping ellipsoidal pores.

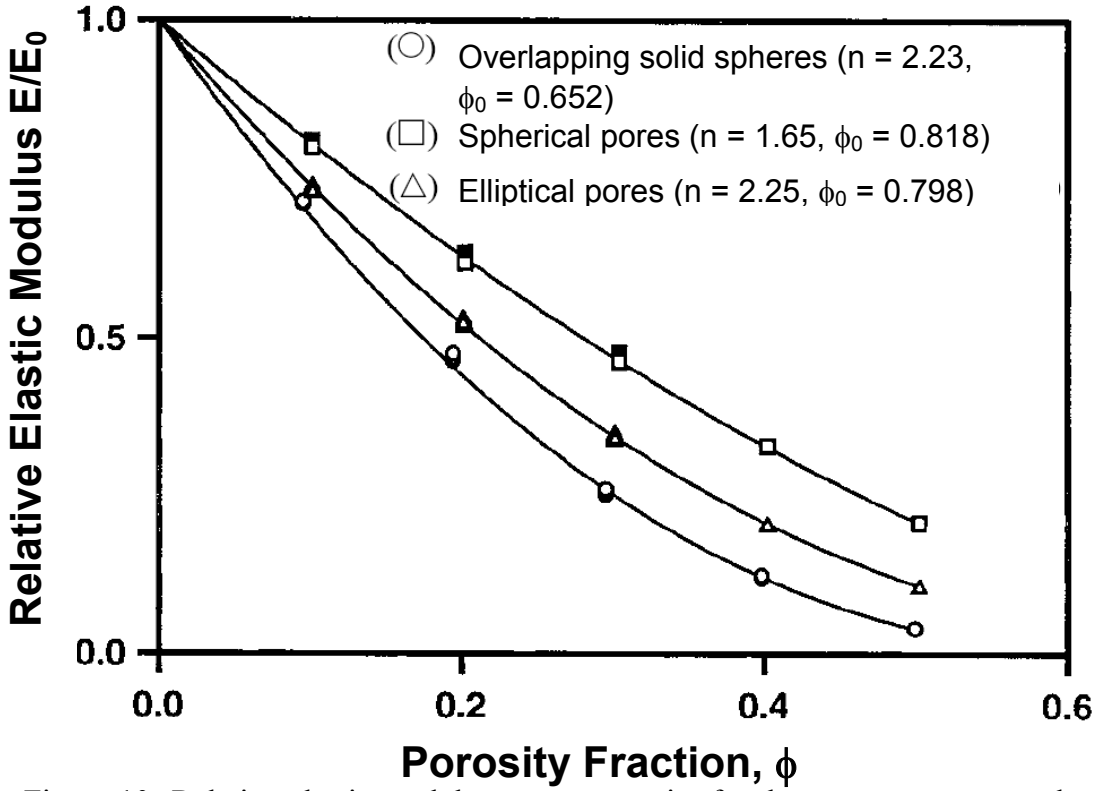


Figure 10 Relative elastic modulus versus porosity for the computer generated porous structures shown in Figure 9 from [27]. Parameters n and $\phi_0$ from Equation (8) given for each structure. Results for solid Poisson ratios $\nu_s$ from -0.1 to 0.4 are plotted at each $\phi$ value and are nearly identical; there is no solid Poisson ratio dependence.

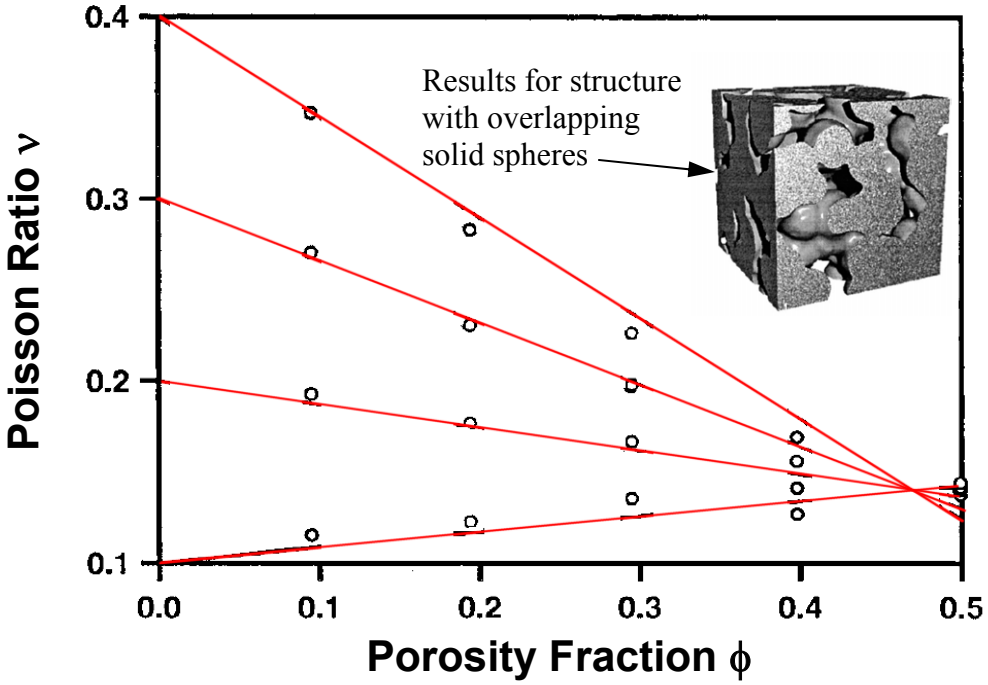


Figure 11 Poisson ratio ν versus porosity fraction ϕ for porous structure with overlapping solid spheres using solid Poisson ratio $\nu_s$ from 0.1 to 0.4 [27]. Linear curve fit using Equation (10) with the asymptotic limiting value of Poisson ratio $\nu_\infty = 0.14$ and the porosity value corresponding to the asymptotic limit $\phi_\infty = 0.472$.

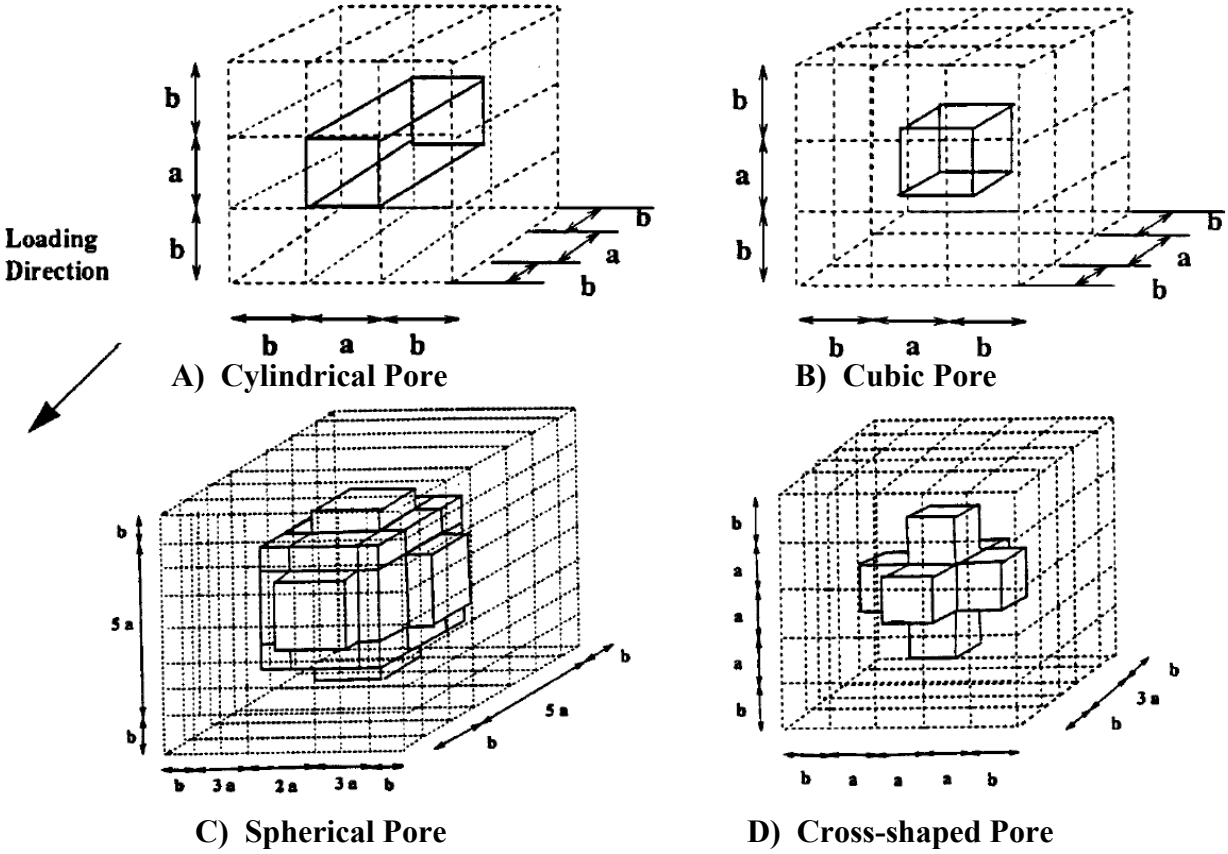


Figure 12 Idealized pore shapes (three dimensional unit cells) analyzed by Herakovich and Baxter [28] to examine the influence of pore geometry and amount on elastic modulus and non-linear tensile response using the generalized method of cells: A) Cylindrical Pore, B) Cubic Pore, C) Spherical Pore, and D) Cross-shaped Pore.

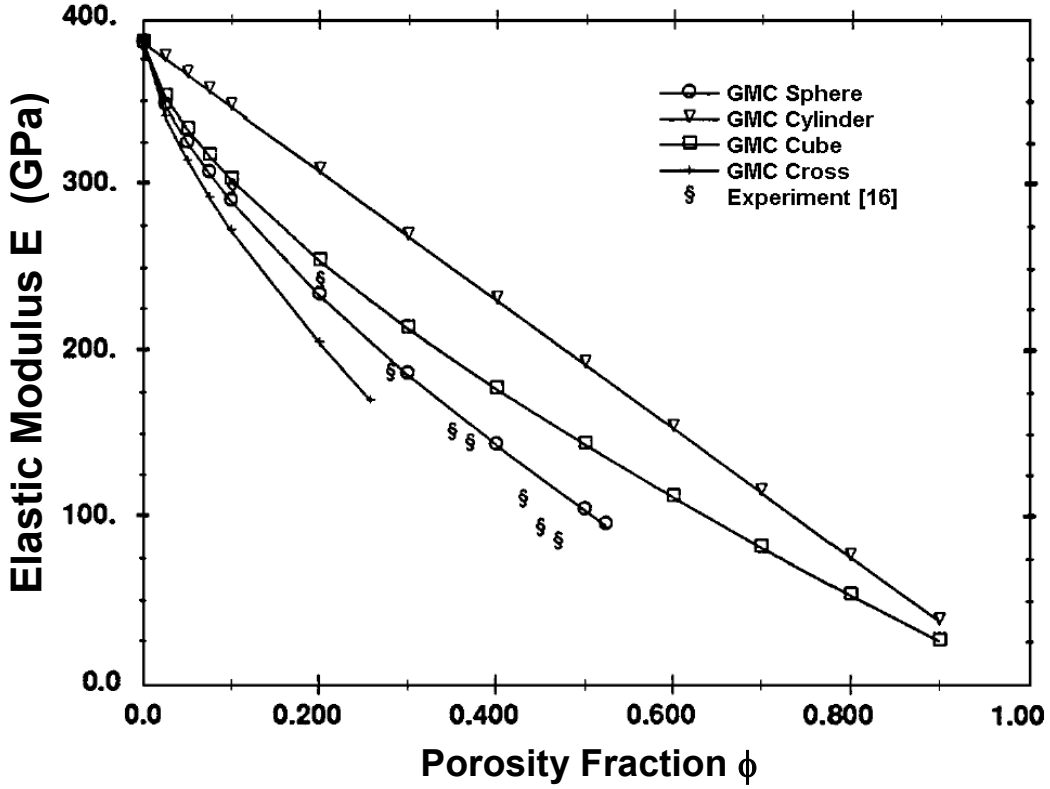


Figure 13 Elastic modulus as a function of porosity fraction $\phi$ for $Al_2O_3$ using the generalized method of cells [28] and experimental data from [16].

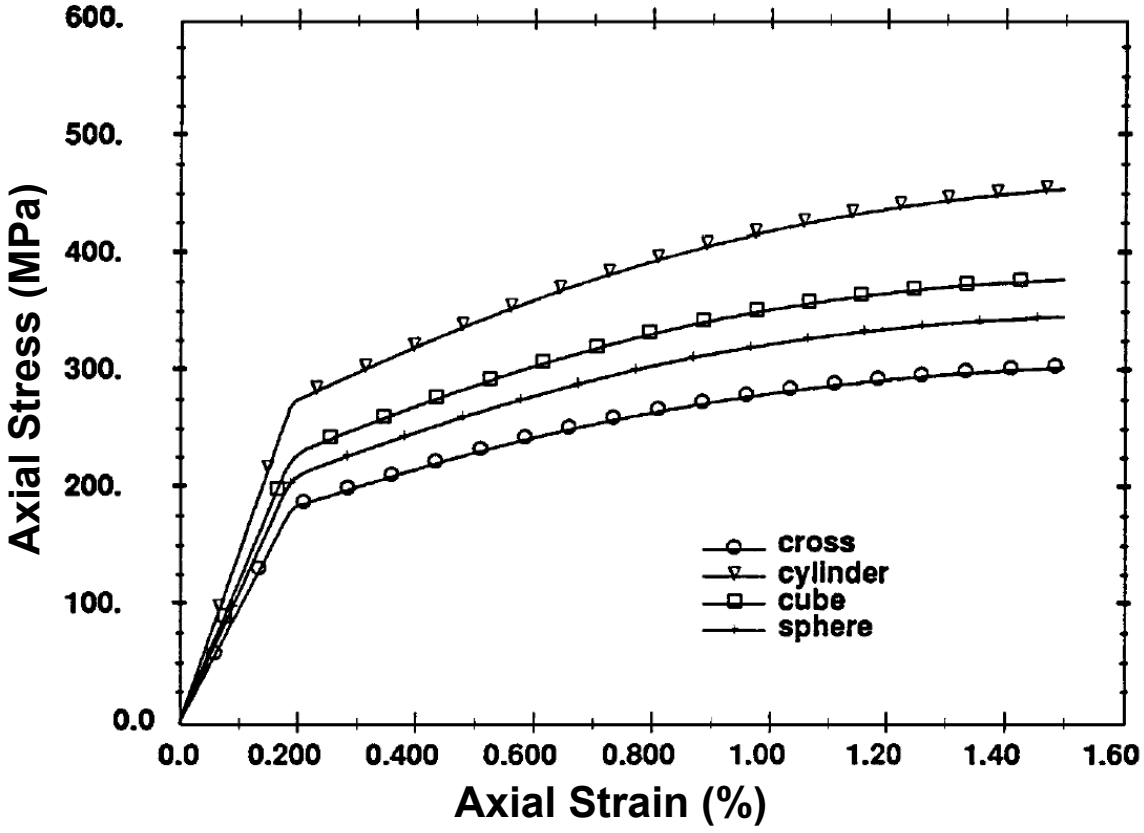


Figure 14 Non-linear tensile response as a function of pore geometry for porosity fraction $\phi$ = 0.2 using the generalized method of cells for the four idealized pore shapes [28].

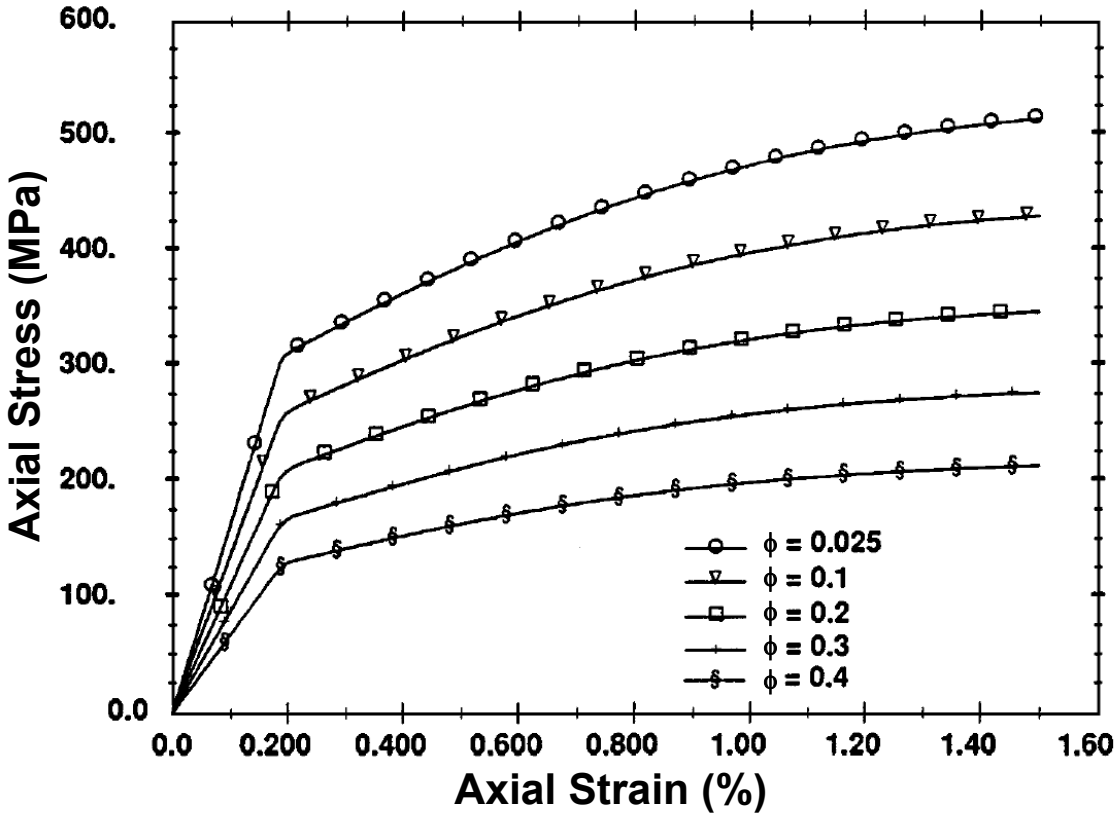


Figure 15 Non-linear tensile response of spherical pore geometry as a function of porosity fraction ϕ using the generalized method of cells [28].

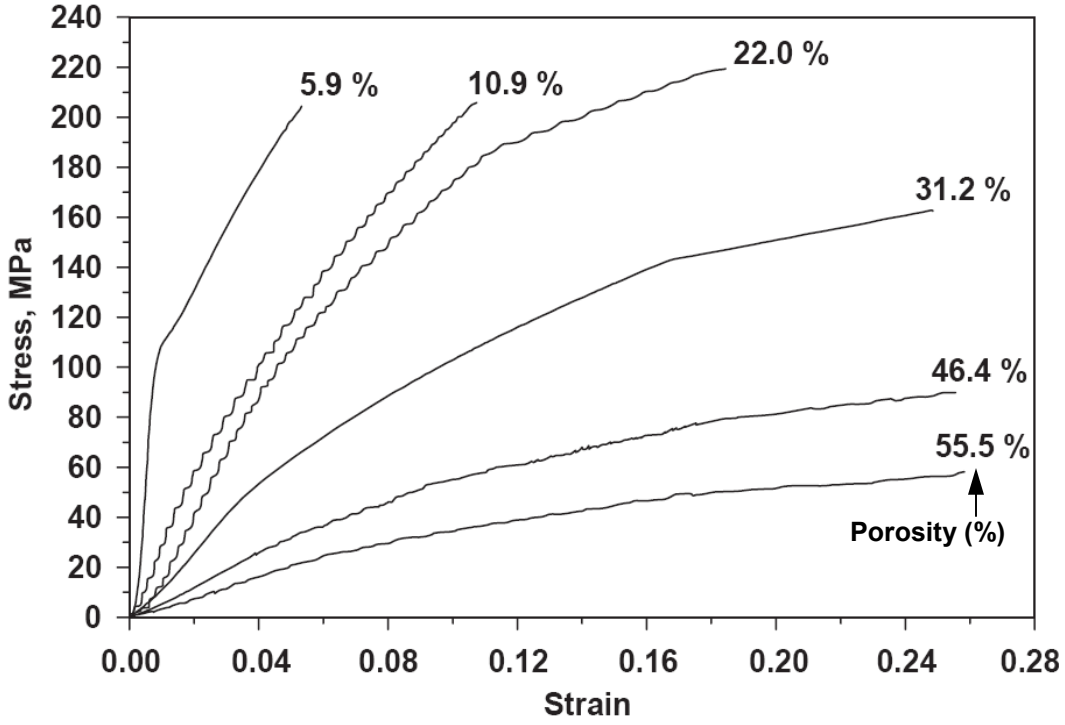


Figure 16 Stress-strain curves for sintered 5 μm copper powder in compression, from 5.9% to 55.5% porosity. Porosity of each curve is indicated at ultimate stress points [9].

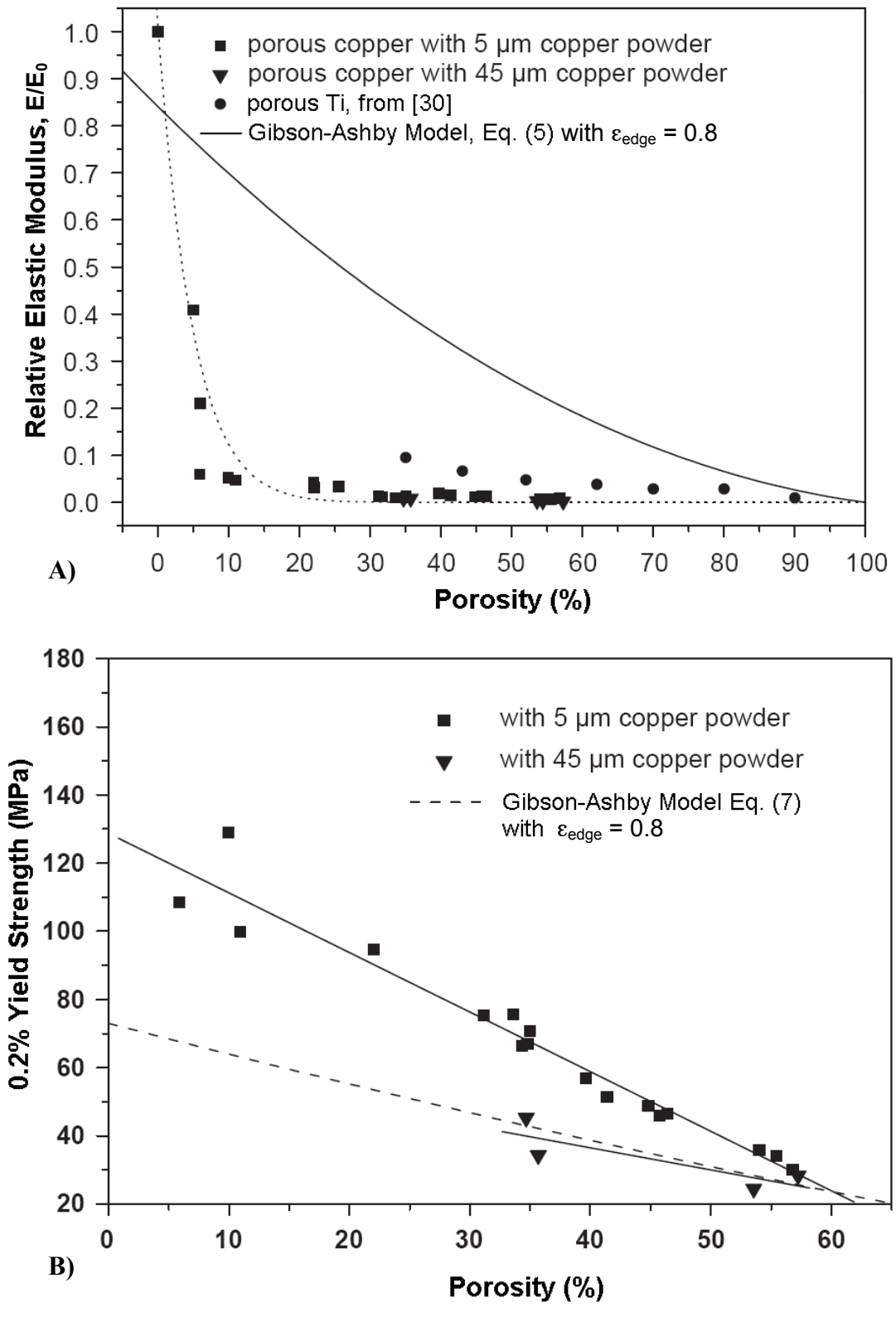


Figure 17 A) Relative elastic modulus versus porosity percentage for sintered copper and titanium experimental data compared with model equation (5). B) 0.2% compressive yield strength versus porosity percentage for sintered copper; experimental data is compared with model Equation (7). Both adapted from [9].

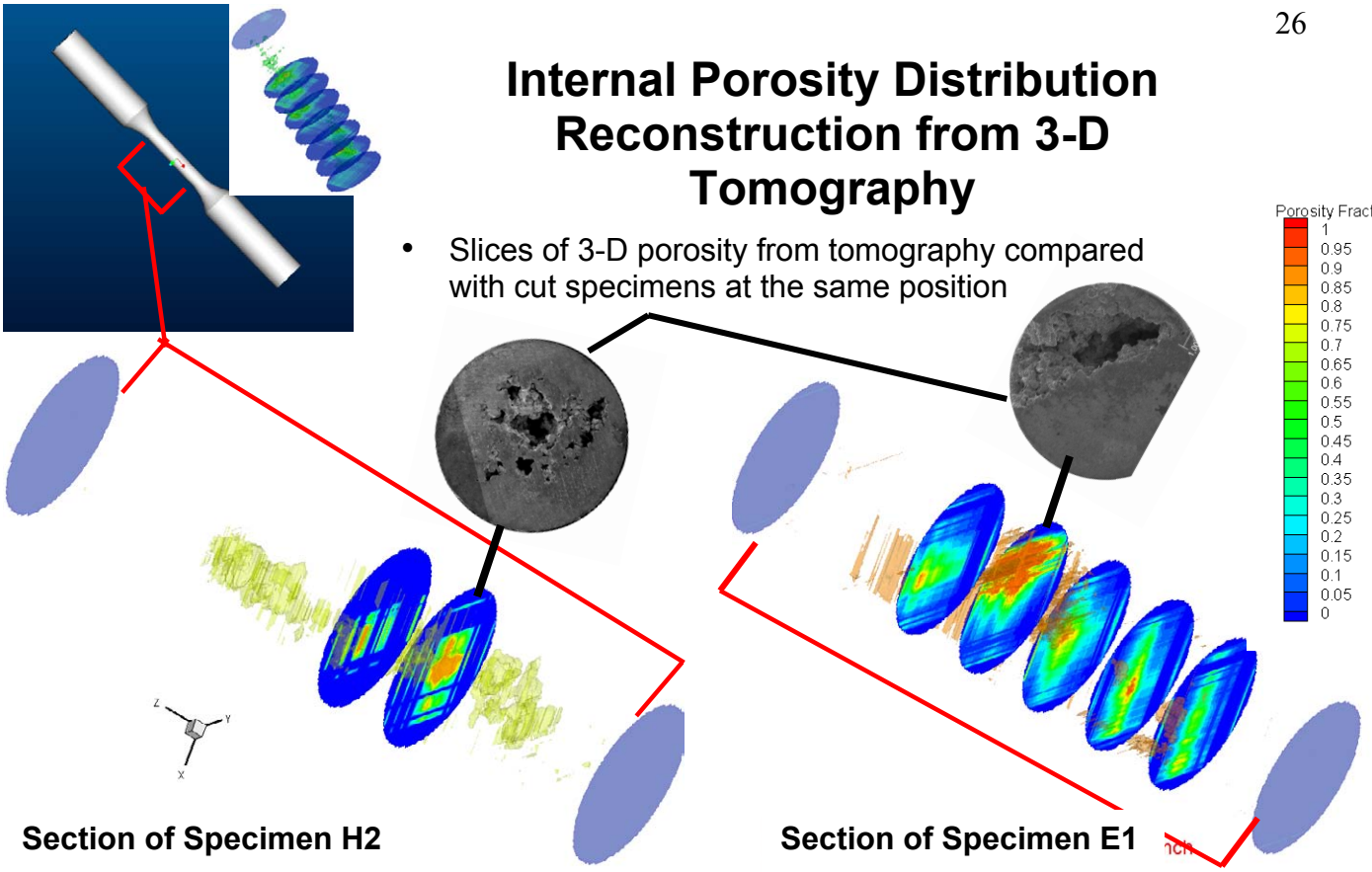


Figure 18 Examples of x-ray tomography results for two fatigue test specimens.

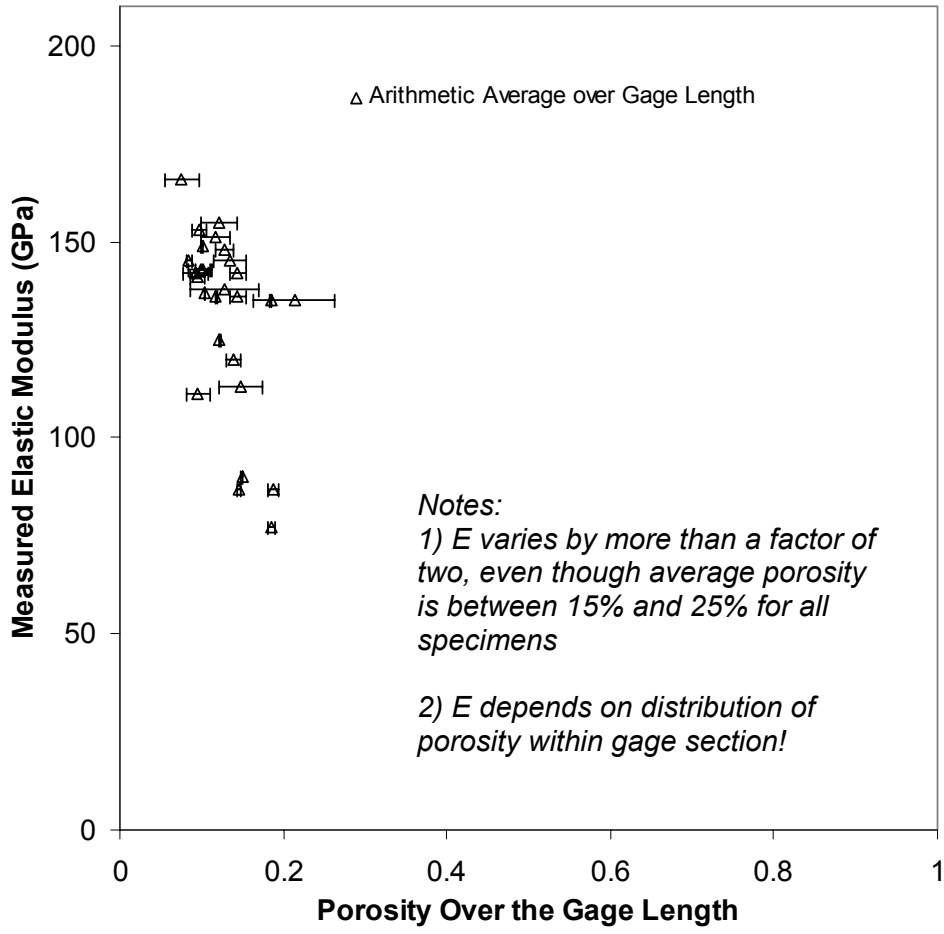


Figure 19 Measured elastic modulus versus average porosity in gage length of test specimens.

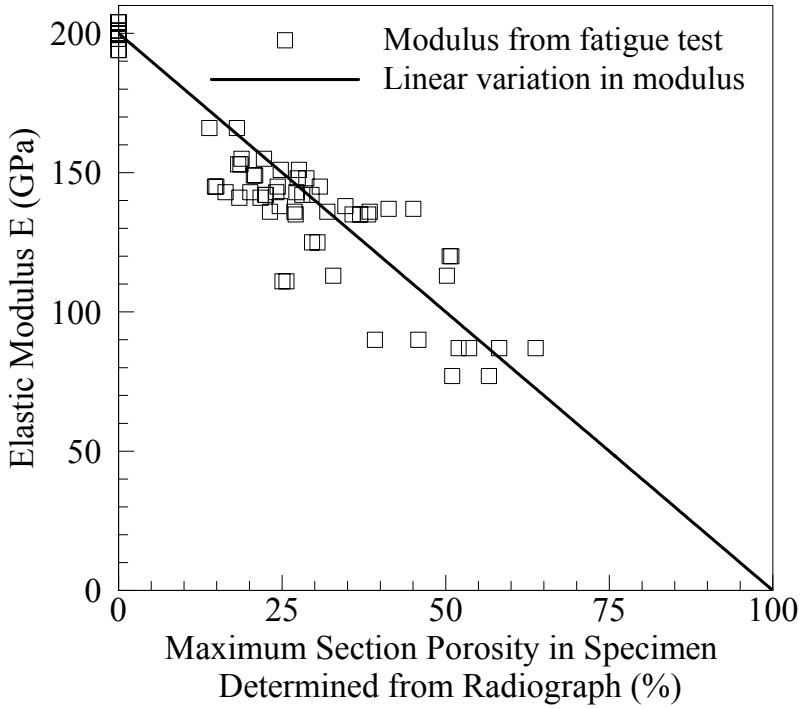


Figure 20 Measured elastic modulus versus maximum section porosity from [6].

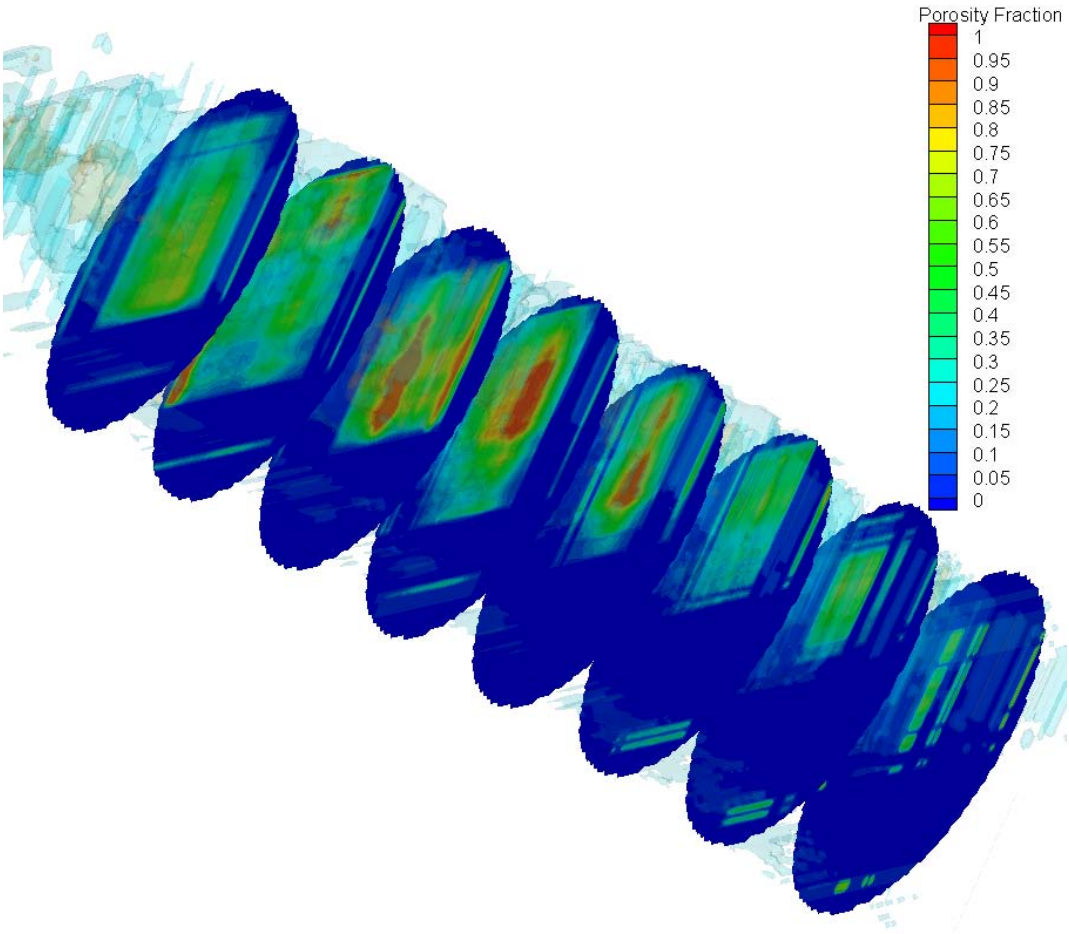


Figure 21 Porosity distribution at longitudinal slices of test specimen H8 from tomography.

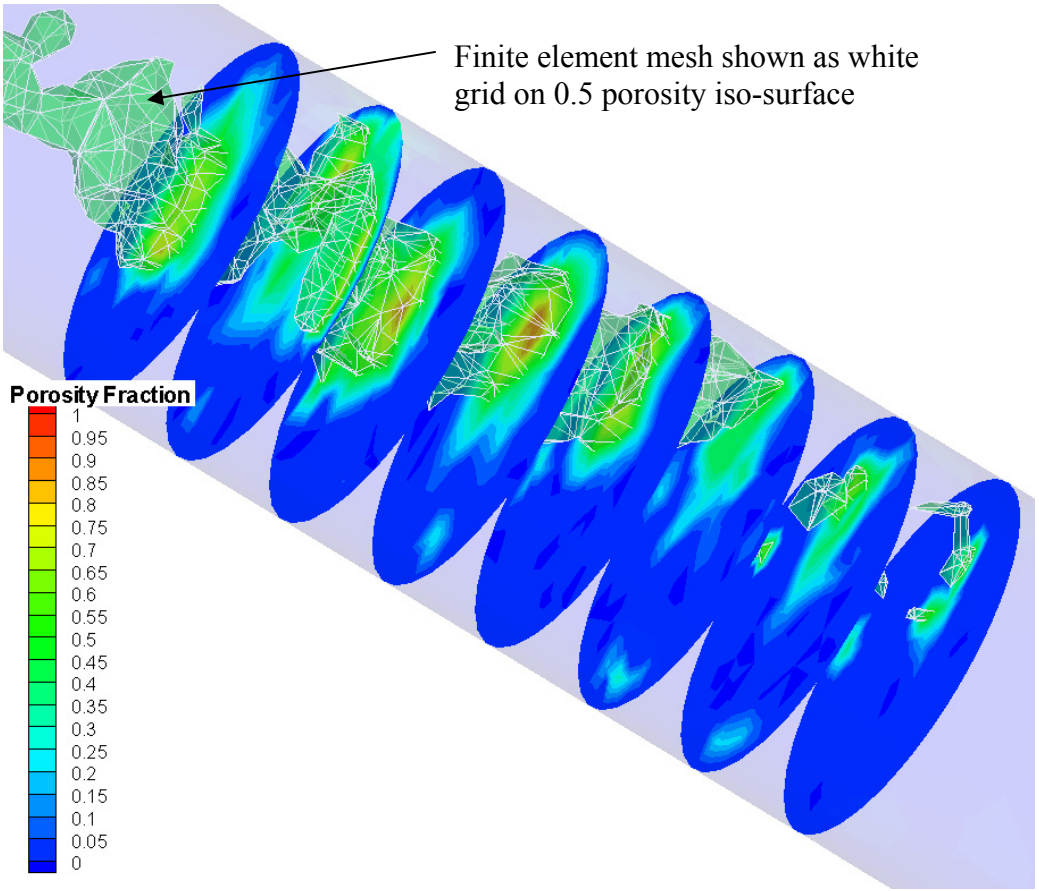


Figure 22 Porosity distribution at longitudinal slices of test specimen H8 from mapping tomography results onto the finite element mesh. Internal structure of mesh shown on 0.5 solid fraction iso-surface to reflect grid coarseness.

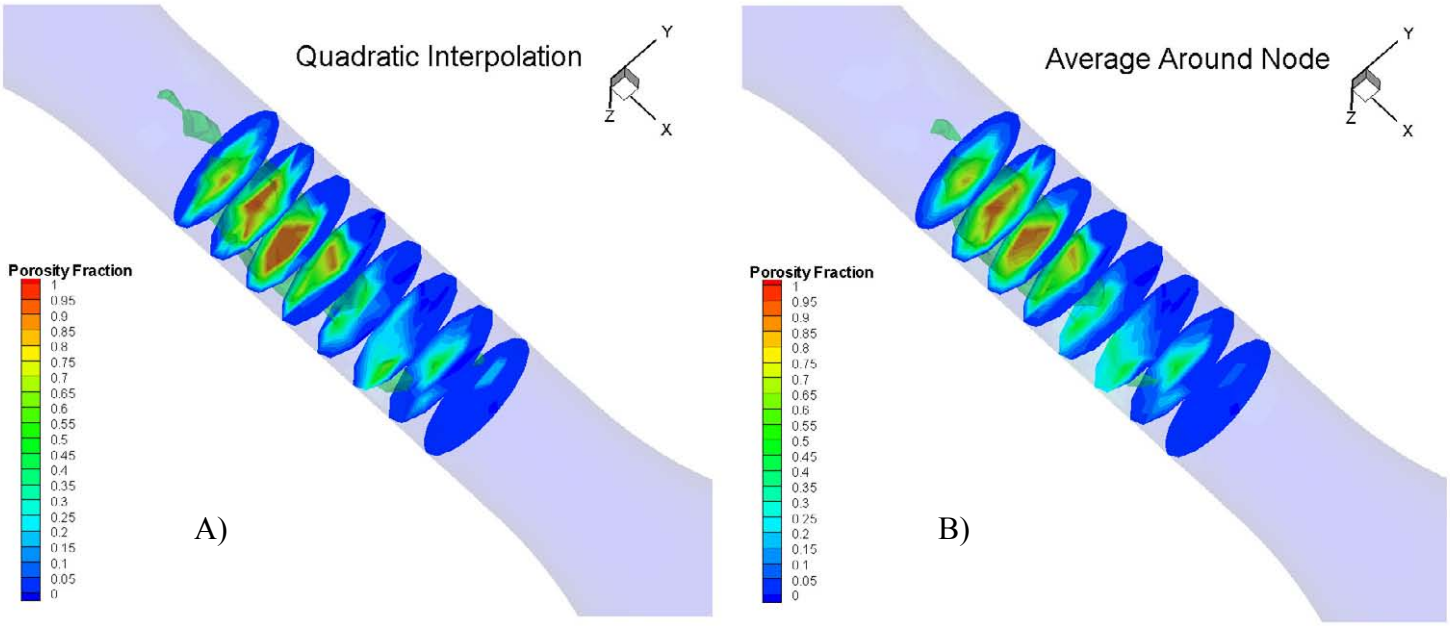


Figure 23 Slices of the same porosity distribution mapped to FEA mesh by two methods A) a 3-D quadratic interpolation method and B) a cubic volume around the FEA mesh node.

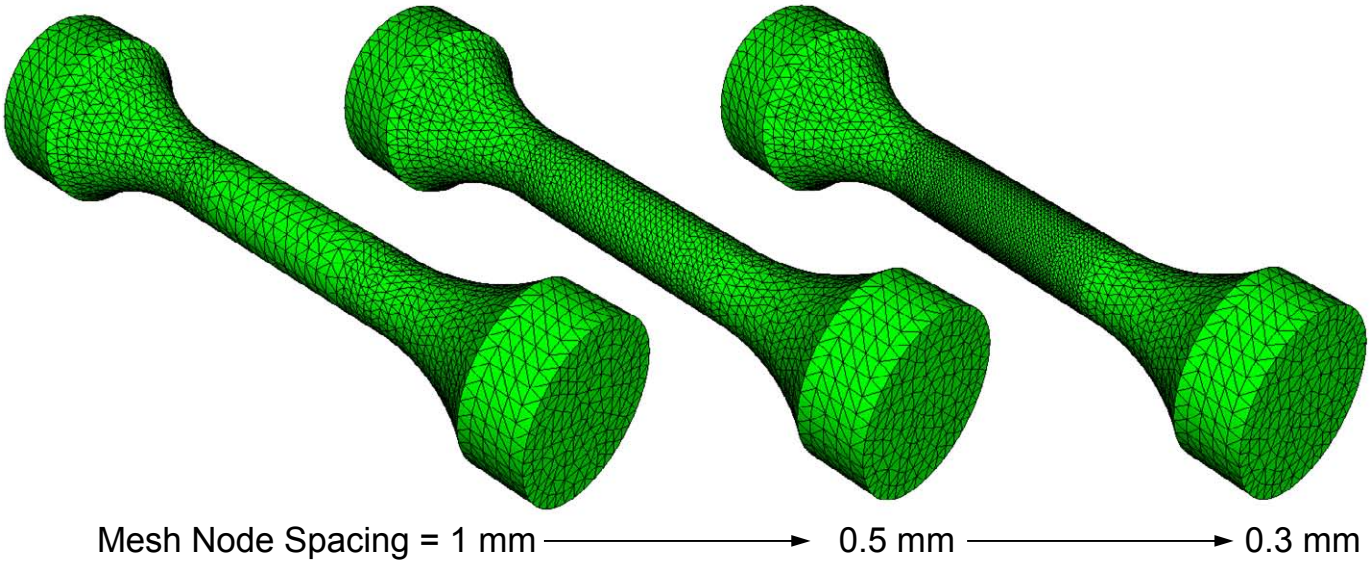


Figure 24 Three example FEA meshes of node spacing 1, 0.5 and 0.3 mm used to study effect of grid coarseness and porosity interpolation method on simulation results.

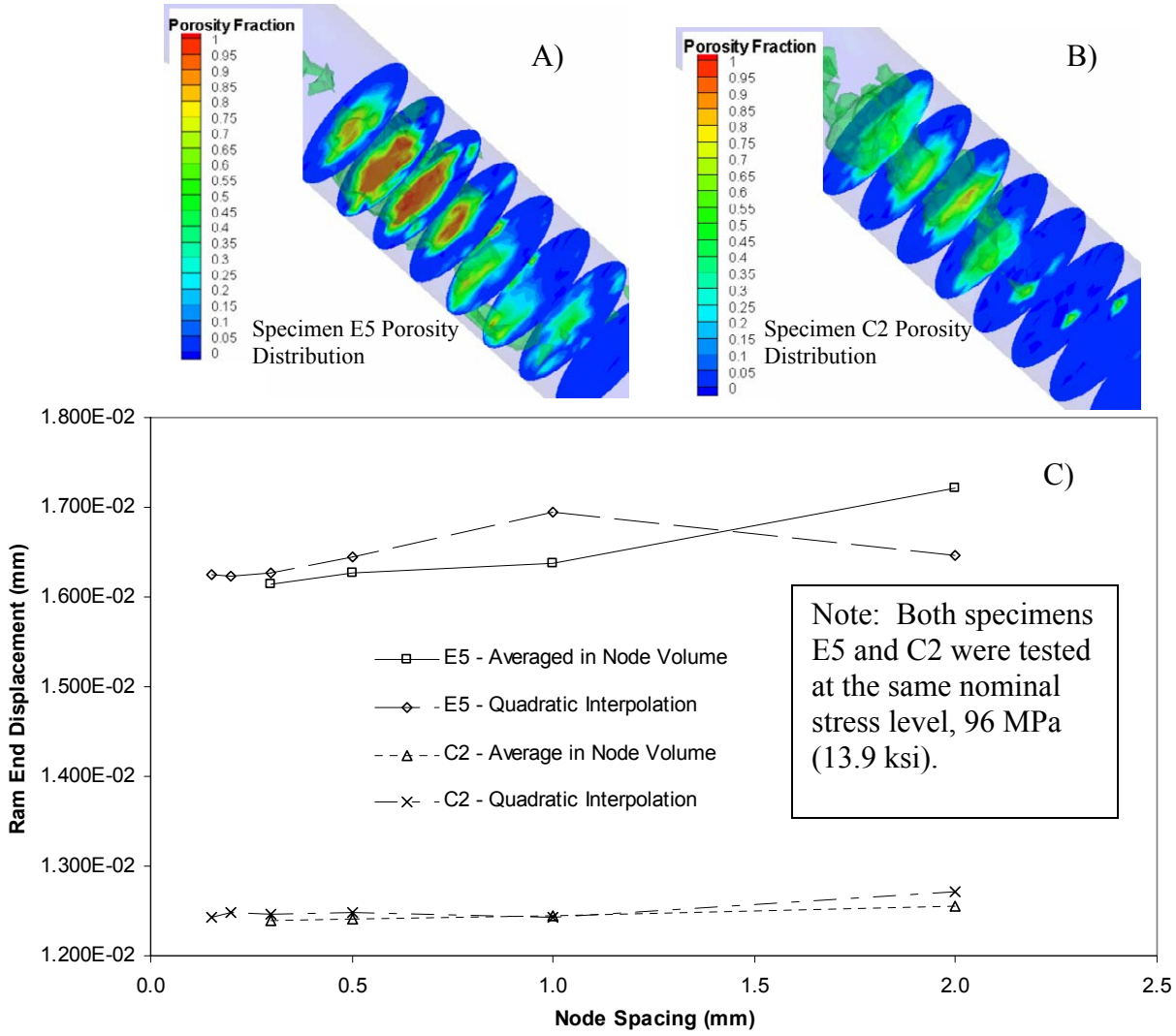


Figure 25 Grid study results for porosity distributions of specimens A) E5 and B) C2 showing FEA simulation results for ram end (or grip end) displacement versus FEA mesh node spacing for the two interpolation methods.

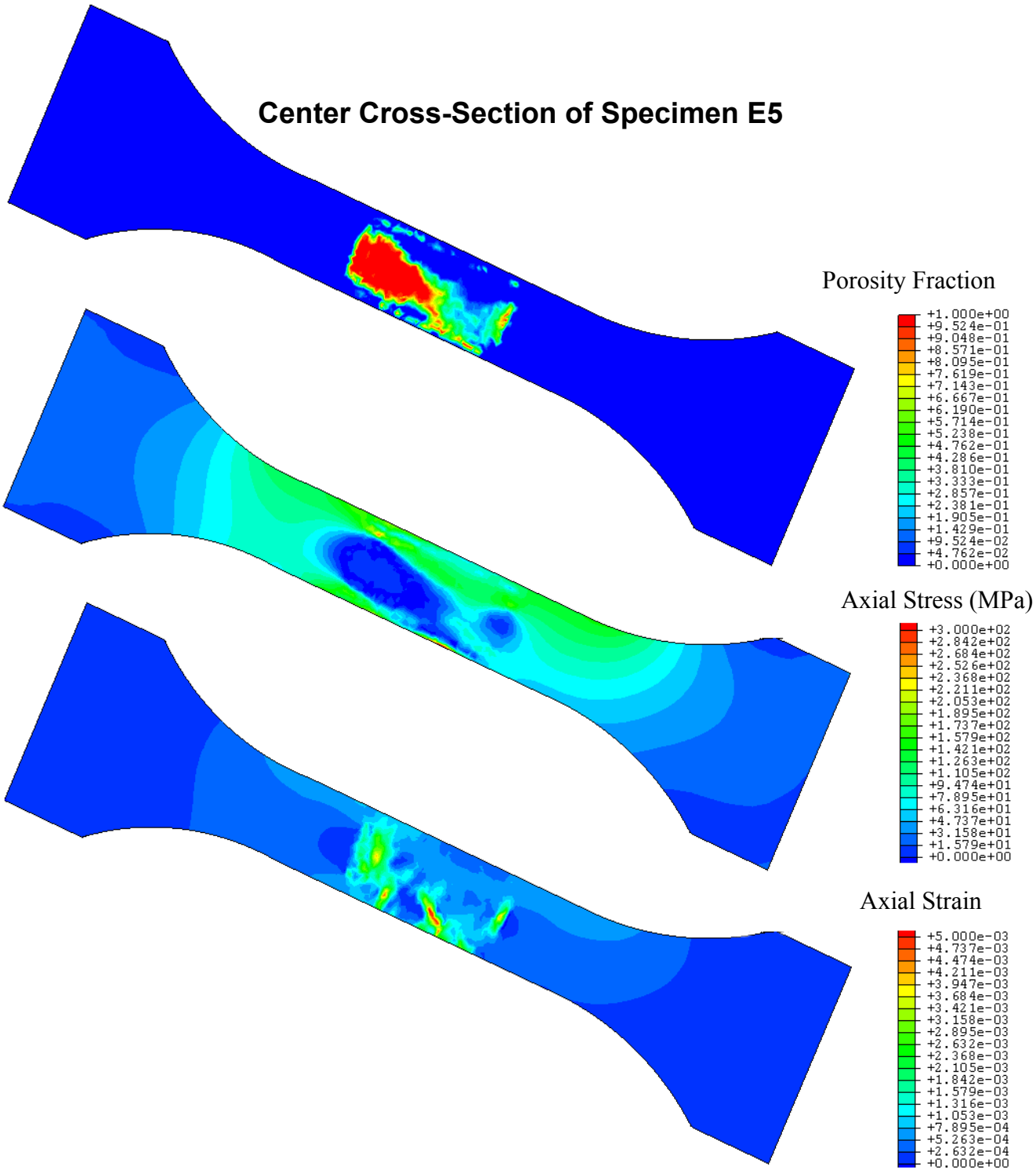


Figure 26 ABAQUS simulation data for Specimen E5. A) Porosity fraction, B) Axial Stress, and C) Axial Strain. Nominal gage section stress is 96 MPa based on a porosity free gage section.

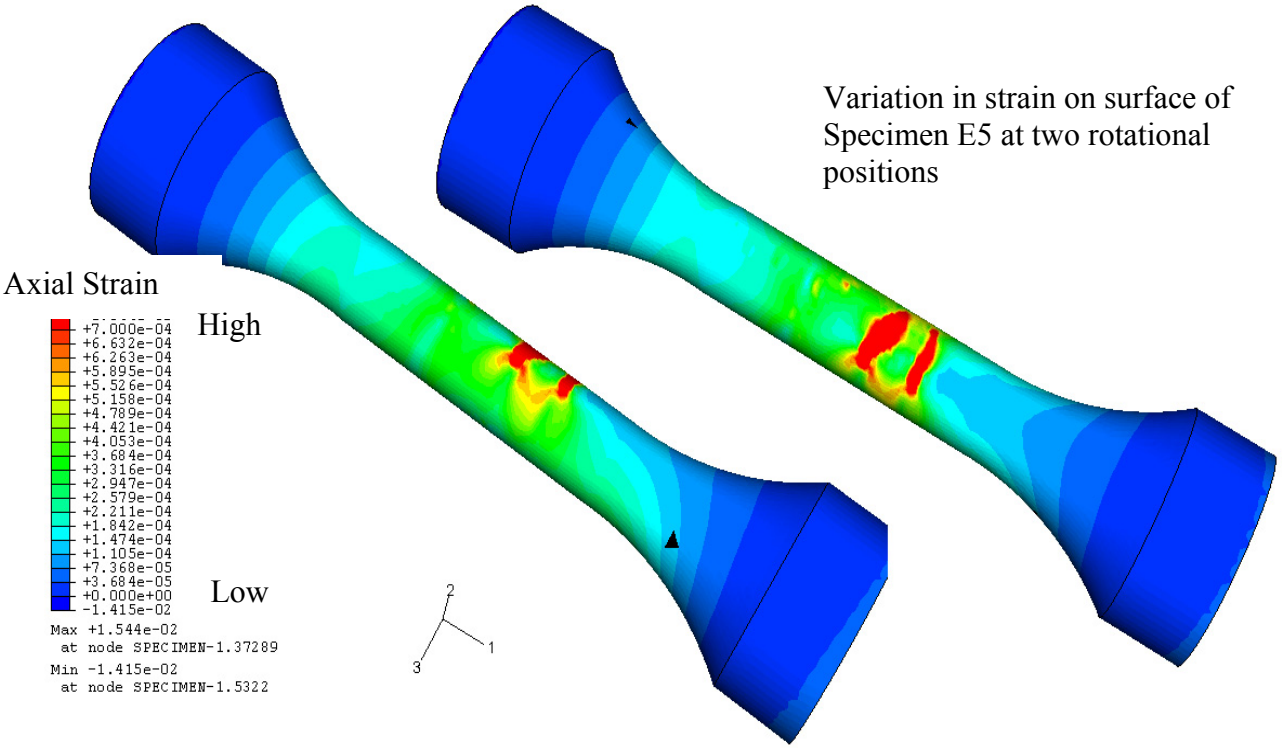


Figure 27 Variation in axial strain on the surface of specimen E5 for two rotated views. In gage section axial strain on surface is shown to vary from 200 to 600 microstrain.

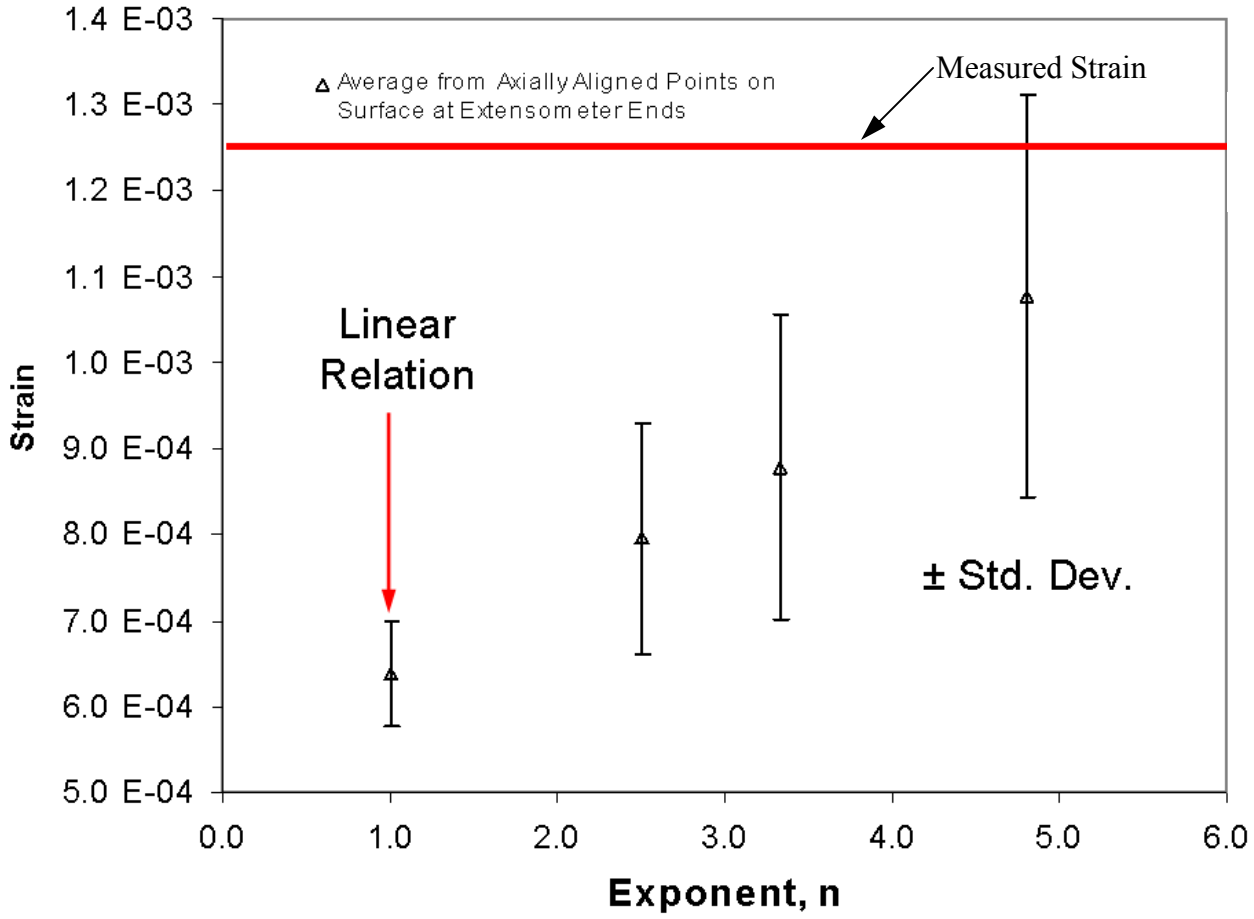


Figure 28 Effect of n on results of strain predictions, using Equation (8) with $\phi_0 = 1.0$ and variable n for Specimen E5 compared with the measured strain.

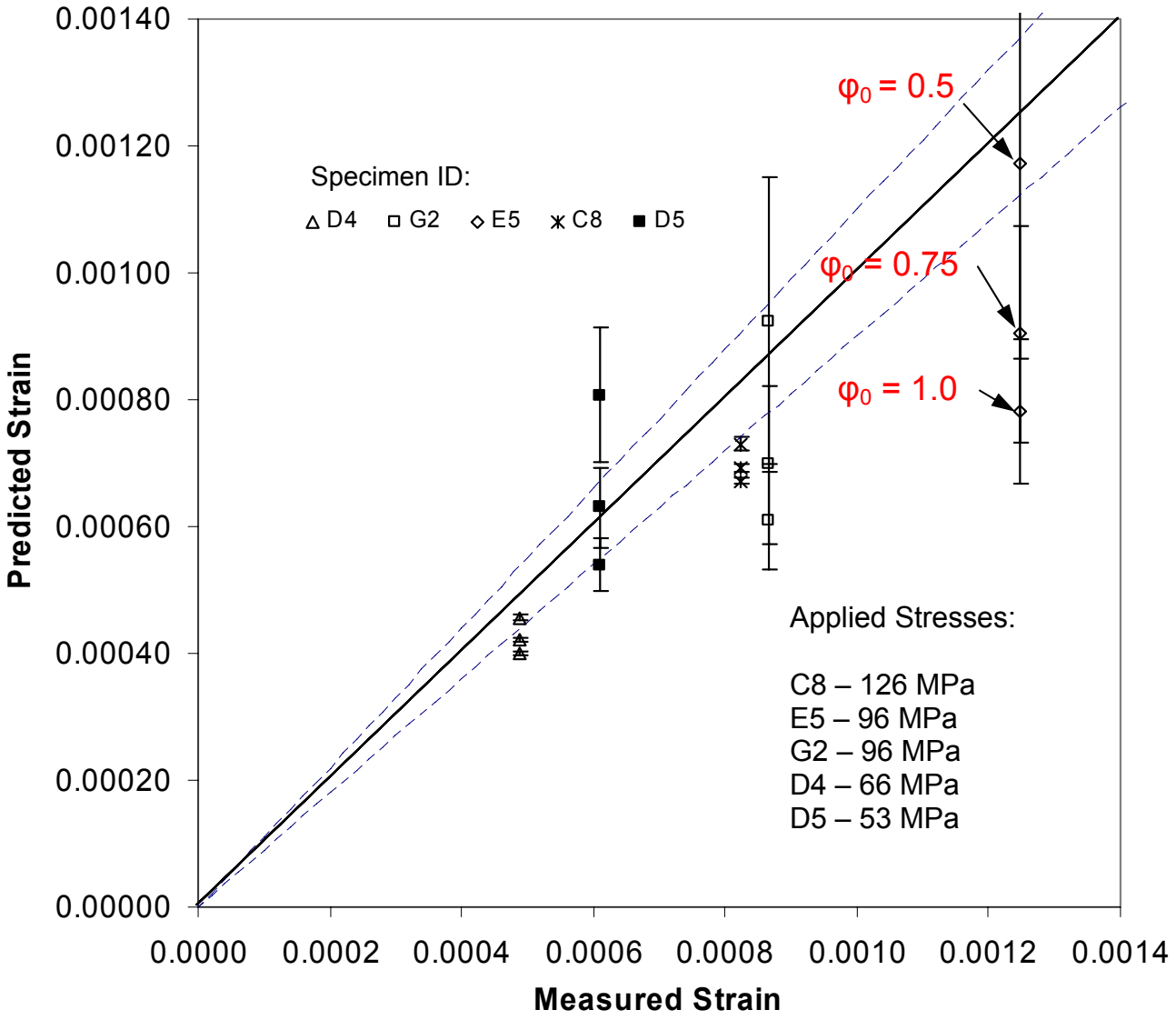


Figure 29 Effect of critical porosity fraction $\phi_0$ on predicted versus measured strain for five specimens, using elastic modulus versus porosity relation Equation (8) with n = 2.25, and critical porosity fraction $\phi_0$ = 1.0, 0.75, and 0.5.

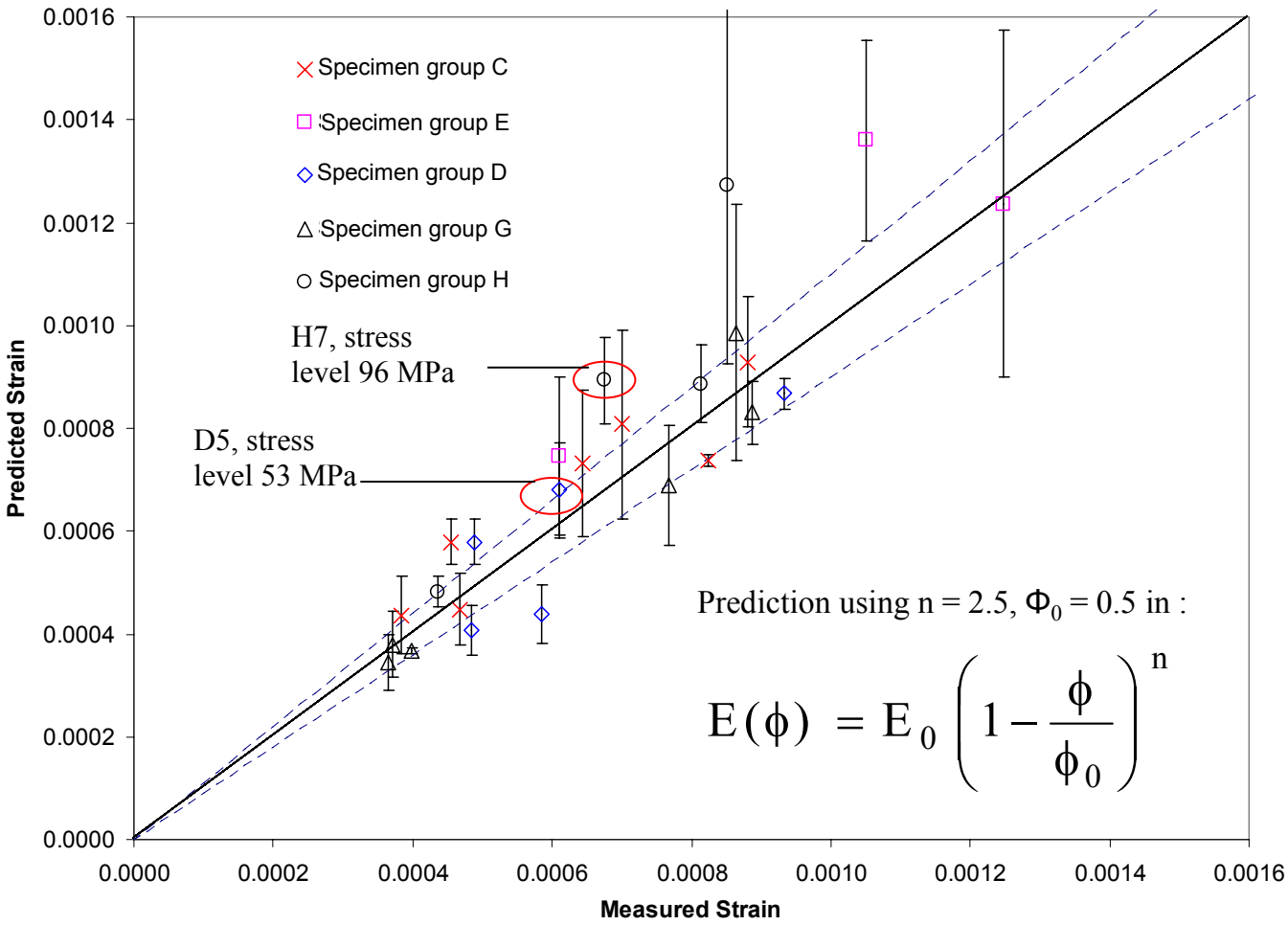


Figure 30 Predicted strain from ABAQUS FEA simulations versus measured strain with simulations using E as function of porosity from Equation (8) with n = 2.5, and critical porosity fraction $\phi_0 = 0.5$. Line of perfect correspondence and ±10% band also plotted.

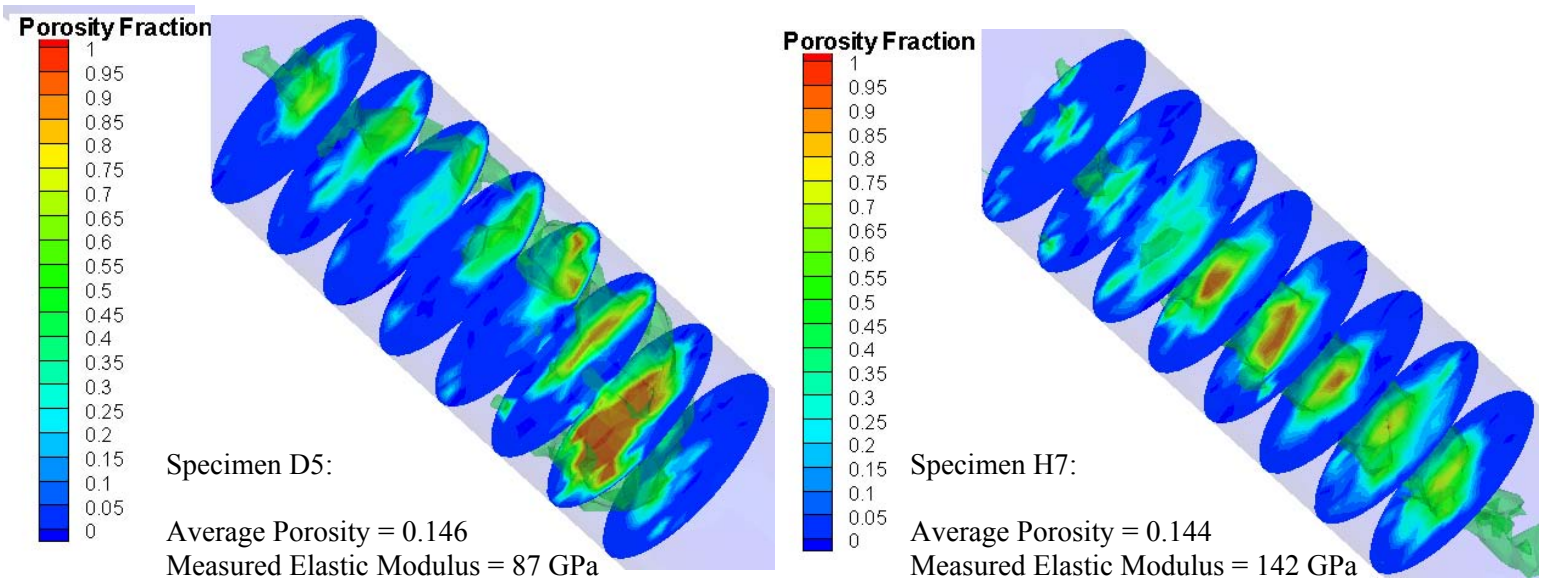


Figure 31 Porosity distributions in slices along gage section in two specimens having the same average porosity and measured E differing by about 40%.

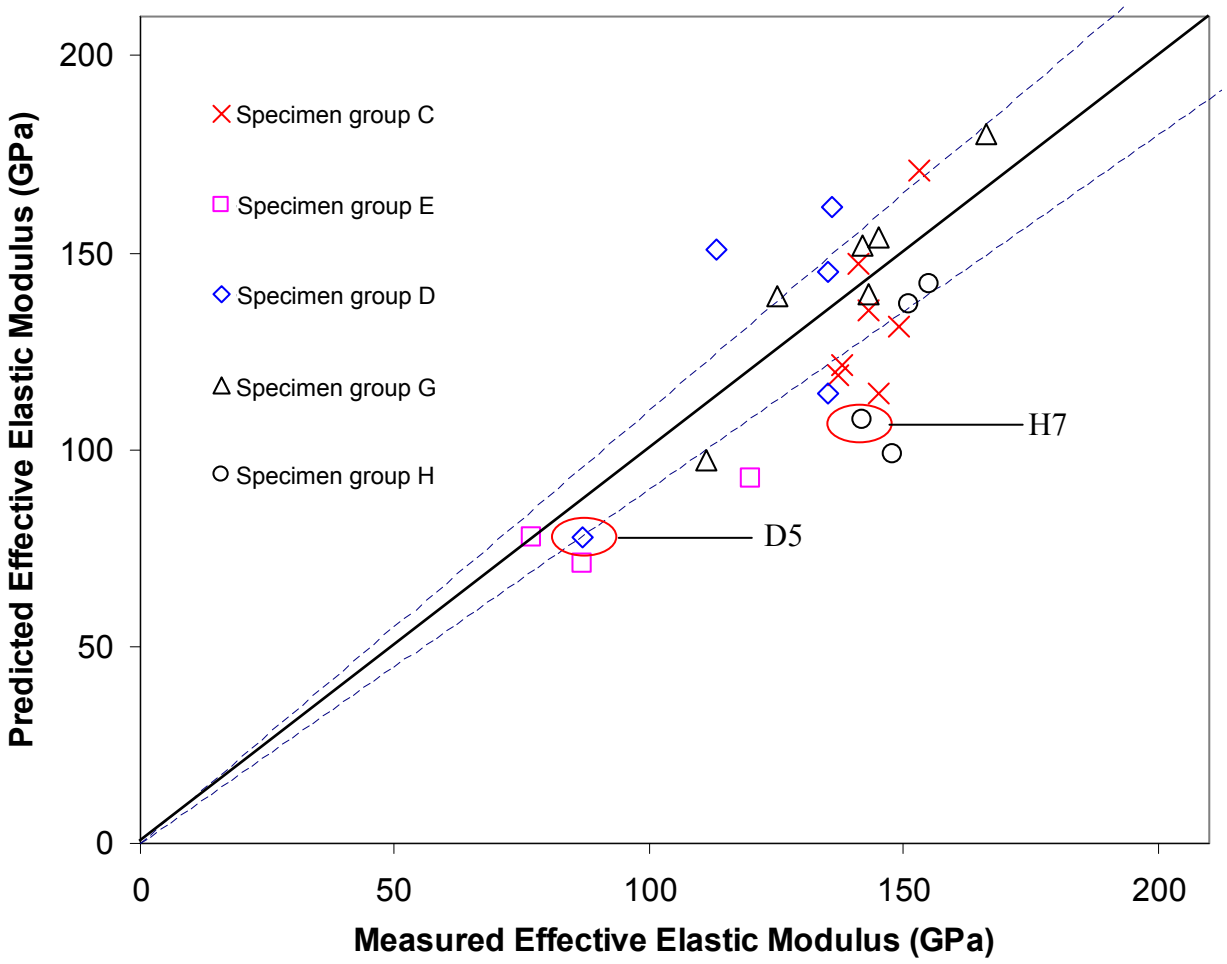


Figure 32 Predicted versus measured elastic modulus with two specimens shown in Figure 31 indicated. Line of perfect correspondence and ±10% band also plotted.